

# Physical effects of water droplets interacting with turbulent premixed flames: A Direct Numerical Simulation analysis

Josef Hasslberger<sup>a,b,\*</sup>, Gulcan Ozel-Erol<sup>c</sup>, Nilanjan Chakraborty<sup>c</sup>, Markus Klein<sup>b</sup>, Stewart Cant<sup>a</sup>

<sup>a</sup>*Department of Engineering, University of Cambridge, Trumpington Street, Cambridge CB2 1PZ, United Kingdom*

<sup>b</sup>*Institute of Applied Mathematics and Scientific Computing, Bundeswehr University Munich, Werner-Heisenberg-Weg 39, 85577 Neubiberg, Germany*

<sup>c</sup>*School of Engineering, Newcastle University, Claremont Road, Newcastle-Upon-Tyne NE1 7RU, United Kingdom*

---

## Abstract

Three-dimensional carrier-phase Direct Numerical Simulations (DNS), combined with a Lagrangian representation of individual droplets, have been employed in this parametric study to examine the physical effects of liquid water mist interacting with laminar and turbulent premixed stoichiometric n-heptane air flames. Significant reductions of flame temperature and burning velocity have been observed in the presence of water droplets. In agreement with the laws governing evaporation, a strongly non-linear influence of the droplet size on the overall burning rate has been noted, whereas the influence of water loading is fairly linear. Different regimes of droplet-flame interaction are known to exist and this has been investigated by numerical experiments focusing on the influence of the latent heat of vaporization. When using realistic fluid properties of water, the cooling effect due to the enthalpy sink of evaporating droplets outweighs the dilution effect due to the local release of steam. Under turbulent conditions, the effectiveness of the droplets in reducing the overall burning rate changes owing to the transient nature of the droplet-flame interaction. Furthermore, it was found that the evaporating droplets significantly diminish the flame-generated

---

\*Corresponding author

*Email address:* josef.hasslberger@unibw.de (Josef Hasslberger)

turbulence and this leads to weaker turbulent wrinkling of the flame surface as compared to gaseous premixed reference simulations without droplets. Based on a comparison of the time scales representing droplet evaporation and [the droplet residence time within the flame](#), a reduced-order model is proposed to account for both the cooling and dilution effects with respect to flame temperature and laminar burning velocity.

*Keywords:* Direct Numerical Simulation, Water droplets, Droplet-flame interaction, Flame-generated turbulence, Cooling and dilution effect

---

## 1. Introduction

The manipulation of combustion processes by liquid water injection has a long tradition. A considerable number of applications or scenarios can be mentioned, ranging from aircraft propulsion to automotive applications and  
5 fire/explosion safety installations. As early as in the 1940s, the DB605D engine of the Messerschmitt BF-109 aircraft used water/methanol injection for a power boost of up to 40% during takeoff and climb. A well-known realization is Pratt & Whitney's J57 jet engine, featuring water injection for takeoff, as installed in the B-52 bomber and KC-135 tanker. Another prominent example is the Rolls-  
10 Royce Pegasus engine, as installed in the Harrier vertical-takeoff-and-landing aircraft.

Before being eventually banned in the 1980s, water/methanol injection was also popular in Formula 1 turbo engines, but is still being applied in rallye (e.g. Subaru WRX) and drag-racing. The most recent realization in volume-produced  
15 cars is BMW's M4 GTS (from 431 to 500 HP and 550 to 600 Nm due to water injection). Bosch also independently offers a system called WaterBoost, yielding up to 5% increase in engine performance, 4% decrease in CO<sub>2</sub> emissions and 13% improvement in fuel economy. Additional effects comprise a shifting of the knocking limits and a reduction of temperature loads on the exhaust gas  
20 catalyst.

Based on experimental investigations of a swirl-stabilized premixed natural

gas burner, Lellek [1] estimated the potential of performance increase in gas turbine engines due to water injection to be about 30%. It has also been concluded that the atomization characteristics of the water spray are of vital importance in terms of pollutant formation (CO and NO<sub>x</sub>), because of the influence of the uniformity of water distribution and the occurrence of hot spots.

Fan et al. [2] added water droplets of 36.6 μm mean size to a premixed methane-air flame in order to investigate the flame suppression effects using a dedicated two-phase PIV technique. A particular focus was placed on the accurate quantification of the slip velocity between the liquid and gaseous phase, which plays an important role in determining both the droplet evaporation rate and residence time within the flame. The results showed that water droplets reduce the flame speed substantially, especially at high strain rates.

The usage of water sprinklers to avoid or mitigate accidental flame propagation is widespread on offshore platforms, in nuclear reactors and in the chemical/process industry. In case of high-speed flame propagation, i.e. explosions, aerodynamic breakup of droplets by impulsively accelerated flow or even shock waves [3] is an important factor since this interaction heavily influences the droplet size distribution and thus the overall burning rate [4]. Thomas [5] further summarized the chemical and physical processes relevant to explosion mitigation by water sprays. It has been emphasized that the major suppression contribution comes from those droplets smaller than 50 μm and that an accurate characterization of the generally poly-disperse spray is essential. In practice, the effectiveness of water sprays also depends on the initial strength of the explosion. The droplet size distribution eventually interacting with the flame can be very different to the unaffected size distribution corresponding to a certain nozzle configuration. To be able to draw clear conclusions, mono-disperse droplets are imposed in the present work but different droplet diameters have been considered.

Another interesting aspect of combustion manipulation by water sprays is related to turbulence generation by the spray itself. In this regard, water nozzles typically installed on offshore platforms have been studied by Van Wingerden

and Wilkins [6]. Under adverse conditions, the flame speeds found in the presence of turbulence due to various types of nozzles were up to 2.3 times the flame speeds without water sprays – which is in contrast to the original intention. The properties of the turbulence appear to be related to the dimensions of the chamber in which the experiments were performed rather than the size of the droplets (e.g. due to vortex shedding). In other applications like internal combustion engines, this enhancement effect may as well be beneficial. The spray-induced turbulence increases the fuel consumption rate while the water droplets are decreasing the flame temperature at the same time.

Zhang et al. [7] also reported on the enhancement effects on methane-air explosions caused by the spraying of water into a sealed vessel. For the investigated Sauter mean diameters of 28.2  $\mu\text{m}$  and 43.3  $\mu\text{m}$  as well as various equivalence ratios, the maximum explosion overpressure, pressure rising rate and flame propagation velocity increased considerably after spraying. Hence, it would be worthwhile to separate the effects of (spray-induced) turbulence from those of the water droplets themselves, as is done in the present work.

Using fully resolved two-dimensional simulations, Nicoli et al. [8] recently examined premixed flame dynamics in the presence of water mist. The droplet inter-distance emerged to be a parameter requiring specific attention. For a small droplet inter-distance, a sufficient amount of water (partially) quenches the flame. For larger droplet inter-distance and suitable droplet size, a flame speed enhancement has been observed which is attributed to Darrieus-Landau instability wrinkling the flame. Such a flame speed promotion in the presence of water droplets is interpreted as a secondary non-linear enhancement of the flame surface area.

Representing the worst-case combustion regime in terms of the pressure loads on the containing structure, detonations propagating into water mist have been studied by Thomas et al. [9]. Stripping of a micro-mist from initially larger droplets in the shock flow field enables energy loss from the wavefront in heating and vapourizing the micro-mist. Application of Shchelkin’s criterion to the detonation quenching mechanism shows that a 20% energy loss from the

wavefront is required for quenching. According to Jarsalé et al. [10], a moderate  
85 decrease of detonation propagation velocity has been observed, whereas the deto-  
nation cell size increases significantly for ethylene-air detonations interacting  
with small water droplets.

In the context of non-premixed hydrocarbon flames interacting with water  
mist, further revealing research is available in the literature. Interactions of  
90 fine droplets of water and water/NaOH solutions with a steady non-premixed  
laminar counterflow methane-air flame have been investigated experimentally  
and numerically by Lazzarini et al. [11]. Inclusion of NaOH in water has been  
shown to significantly enhance the fire suppression ability of water by comple-  
menting its thermal effects with chemical catalytic radical recombination effects  
95 of NaOH. Also, fine water mist has been found to be as effective as the now  
banned gaseous fire suppressant Halon 1301. Arias et al. [12] presented a compu-  
tational study on non-premixed flame extinction by water spray. A comparison  
of various simulation cases of two-dimensional ethylene-air counterflow diffu-  
sion flames highlights the flame weakening characteristics due to aerodynamic  
100 stretch and heat loss due to water spray evaporation.

For general interest, it shall also be mentioned that further analysis on hy-  
drogen flames interacting with water mist is available in the literature but these  
contributions are not reviewed here due to the focus on hydrocarbon fuels.

Water is an exceptional substance in many ways. It is characterized by a  
105 very high gas-liquid density ratio as well as the highest specific heat and latent  
heat of vaporization of all liquids (cf. Table 2). Particularly because of this last  
property (and because it is readily available), water is utilized in internal com-  
bustion engines and gas turbine engines as an enthalpy sink to reduce the flame  
temperature. The second main purpose is to boost temporarily the power out-  
110 put/thrust, as in aircraft propulsion, via an increased mass/volume flux through  
the system. In turn, these advantages imply various consequences on fuel effi-  
ciency, emissions, component loads and so forth. From a point of view of the  
underlying phenomena, physical effects and effects related to chemical kinetics  
can generally be distinguished. In terms of the physical effects, the aforemen-

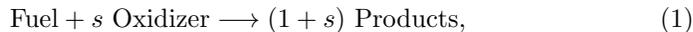
tioned cooling effect due to droplet evaporation and the dilution/concentration effect due to steam generation are particularly relevant in the context of this work. As can be seen from the Arrhenius-type reaction rate expression in Eq. 2, both the fuel and oxidizer concentration as well as the temperature are directly affecting the local burning rate. Unlike strictly inert gases like helium, nitrogen or argon, steam is known to exhibit a non-vanishing chemical effect due to its high third-body efficiency [13, 14]. However, the chemical effect is considered a higher-order effect compared to the physical effects and thus is not investigated in this work. Moreover, the low steam concentrations occurring within the flame (as demonstrated later) justify this approach.

The aforementioned experimental and numerical studies are mostly focused on a global characterization of the combustion process, without a detailed view on the local flame-turbulence-droplet interaction mechanisms. The present work addresses this gap and attempts to isolate the different physical effects by means of Direct Numerical Simulations (DNS). The computational setup represents an idealized configuration but is also relevant to the applications mentioned above. Since the volatility of fuel droplets is much higher than of water droplets, significant pre-evaporation ahead of the flame occurs for fuel droplets, whereas marginal pre-evaporation occurs for water droplets after injection into the combustion chamber. As a consequence, the water vapor concentration ahead of the flame is very low and the local situation (i.e. on the scale that can be captured by the DNS domain) in terms of droplet-flame interaction is represented by the idealized configuration consisting of a gaseous premixed flame interacting with mono-disperse liquid water droplets.

The goals of this study are to improve the fundamental understanding of water droplet flame interaction in a turbulent environment, to isolate the different physical effects and, eventually, to exploit these observations in the sense of a reduced-order modelling strategy.

## 2. Mathematical background

Although three-dimensional DNS with detailed chemistry are generally possible nowadays, e.g. [15, 16], they still remain extremely expensive for heavy hydrocarbons (e.g. n-heptane). Also, an extensive parametric analysis as conducted in this study would be prohibitively expensive for detailed chemistry based DNS (actually orders of magnitude higher in terms of CPU hours). As this paper focuses on the physical effects of water flame interaction, a computationally inexpensive modified single-step irreversible Arrhenius-type chemical reaction has been adopted. Based on a mass balance, the chemical reaction can be formulated in a generic manner as



i.e. 1 unit of fuel +  $s$  units of oxidizer give rise to  $(1 + s)$  units of products, where  $s$  is the stoichiometric mass ratio [17]. The chemical effect of steam is assumed to be a higher order effect compared to the physical effect of steam. Other complex phenomena in terms of chemical kinetics, like ignition, are also not relevant to this study. Accordingly, the fuel reaction rate is given by the Arrhenius-type expression

$$\dot{\omega}_F = -\rho B^* Y_F Y_O \exp\left(\frac{-\beta(1-T)}{1-\alpha(1-T)}\right), \quad (2)$$

based on the gas density  $\rho$ , normalized pre-exponential factor  $B^*$ , fuel mass fraction  $Y_F$ , oxygen mass fraction  $Y_O$ , Zel'dovich number  $\beta$ , heat release related parameter  $\alpha = \tau/(1+\tau)$  and non-dimensional temperature  $T = (\hat{T}-T_0)/(T_{ad}-T_0)$ , where  $\hat{T}$  is the instantaneous dimensional temperature and  $T_{ad}$  is the adiabatic flame temperature. The unburned gas temperature is taken to be  $T_0 = 300 \text{ K}$ , which yields a heat release parameter of  $\tau = (T_{ad}-T_0)/T_0 = 6.54$  in the case of stoichiometric n-heptane air combustion. To account for the generally inhomogeneous mixture distribution due to the localized release of steam (and therefore localized reduction of fuel and oxygen mass fraction), the heat of combustion, activation energy and Zel'dovich number are taken to be functions of the local

equivalence ratio according to the methodology proposed by Fernández-Tarrazo  
 170 et al. [18]. The chemical mechanism has been shown to compare favorably with  
 both experiments and detailed chemistry simulations for typical hydrocarbon-air  
 mixtures [18, 19].

The two-way coupled Euler-Lagrange approach adopted in this work essen-  
 tially follows the pioneering work of Reveillon and Vervisch [20] and has been  
 175 applied in many other recent studies on spray combustion [21, 22, 23, 24, 25].  
 The position, velocity, diameter and temperature of Lagrangian droplets (sub-  
 script  $d$ ) are governed by

$$\frac{d\vec{x}_d}{dt} = \vec{u}_d; \quad \frac{d\vec{u}_d}{dt} = \frac{\vec{u}(\vec{x}_d, t) - \vec{u}_d}{\tau_d^u}; \quad \frac{da_d^2}{dt} = -\frac{a_d^2}{\tau_d^p}; \quad \frac{dT_d}{dt} = \frac{\hat{T}(\vec{x}_d, t) - T_d - \text{B}_d L_v / C_p^g}{\tau_d^T}, \quad (3)$$

where  $L_v$  is the latent heat of vaporization, and  $\tau_d^u$ ,  $\tau_d^p$  and  $\tau_d^T$  are the corre-  
 sponding relaxation time scales:

$$\tau_d^u = \frac{\rho_d a_d^2}{18 C_u \mu}; \quad \tau_d^p = \frac{\rho_d a_d^2}{4 \mu} \frac{\text{Sc}}{\text{Sh}_c \ln(1 + \text{B}_d)}; \quad \tau_d^T = \frac{\rho_d a_d^2}{6 \mu} \frac{\text{Pr}}{\text{Nu}_c} \frac{\text{B}_d}{\ln(1 + \text{B}_d)} \frac{C_p^l}{C_p^g}. \quad (4)$$

180 These expressions are depending on the droplet density  $\rho_d$ , Schmidt number  
 $\text{Sc}$ , specific heat of the liquid phase  $C_p^l$ , corrected drag coefficient  $C_u = 1 +$   
 $\text{Re}_d^{2/3}/6$ , droplet Reynolds number  $\text{Re}_d = \rho |\vec{u}(\vec{x}_d, t) - \vec{u}_d| a_d / \mu$ , Spalding number  
 $\text{B}_d = (Y_W^s - Y_W(\vec{x}_d, t)) / (1 - Y_W^s)$ , and corrected Sherwood and Nusselt numbers  
 $\text{Sh}_c = \text{Nu}_c = 2 + 0.555 \text{Re}_d \text{Sc} / (1.232 + \text{Re}_d \text{Sc}^{4/3})^{1/2}$ , where  $Y_W^s$  is the value  
 185 of the water mass fraction  $Y_W$  at the surface of the droplet. To evaluate the  
 Spalding number  $\text{B}_d$ , the Clausius-Clapeyron equation for the partial pressure  
 of the water vapour at the droplet surface  $p_W^s$  is used according to

$$p_W^s = p_{\text{ref}} \exp\left(\frac{L_v}{R} \left(\frac{1}{T_{\text{ref}}^s} - \frac{1}{T_d^s}\right)\right); \quad Y_W^s = \left(1 + \frac{W_g}{W_W} \left(\frac{p(\vec{x}_d, t)}{p_W^s} - 1\right)\right)^{-1}, \quad (5)$$

where  $R$  is the gas constant,  $T_{\text{ref}}^s$  is the boiling point of the water at pressure  
 $p_{\text{ref}}$  and  $T_d^s$  is assumed to be  $T_d$ .  $W_g$  and  $W_W$  are the molecular weights of the  
 190 gaseous mixture and water, respectively. The two-way coupling between liquid  
 and gaseous phases is realized via additional source terms in the gaseous phase

transport equations

$$\frac{\partial(\rho\varphi)}{\partial t} + \frac{\partial(\rho u_j \varphi)}{\partial x_j} = \frac{\partial}{\partial x_j} \left( R_\varphi \frac{\partial \varphi^*}{\partial x_j} \right) + \dot{\omega}_\varphi + \dot{S}_g + \dot{S}_\varphi, \quad (6)$$

where  $\varphi = \{1, u_i, e, Y_F, Y_O, Y_W\}$  and  $\varphi^* = \{1, u_i, \hat{T}, Y_F, Y_O, Y_W\}$  for the con-  
 195 servation equations of mass, momentum, energy and mass fractions, respec-  
 tively. The  $\dot{\omega}_\varphi$  term corresponds to reaction rate,  $\dot{S}_g$  stands for an appropriate  
 source/sink term in the gaseous phase (e.g. pressure forces in the momentum  
 equation) and

$$\dot{S}_\varphi = -\frac{1}{\Delta V} \sum_d \frac{d(m_d \varphi_d)}{dt} \quad (7)$$

is the source term due to droplet evaporation, which is tri-linearly interpolated  
 from the droplet sub-grid position  $\vec{x}_d$  to the eight surrounding grid points. Here,  
 200  $\Delta V$  denotes the cell volume and  $m_d = \rho_d \pi a_d^3 / 6$  denotes the droplet mass. Based  
 on the kinematic viscosity  $\nu$  and appropriate Schmidt numbers  $\sigma_\varphi$  corresponding  
 to  $\varphi$ ,  $R_\varphi = \rho\nu/\sigma_\varphi$  for  $\varphi = \{1, u_i, Y_F, Y_O, Y_W\}$  and  $R_\varphi = \lambda$  for  $\varphi = e$ . The Lewis  
 numbers of all species are assumed to be unity and all species in the gaseous  
 phase are taken to be perfect gases. Standard values are considered for the ratio  
 205 of specific heats ( $\gamma = C_p^g/C_v^g = 1.4$ , where  $C_p^g$  and  $C_v^g$  are the gaseous specific  
 heats at constant pressure and volume, respectively) and Prandtl number ( $Pr =$   
 $\mu C_p^g/\lambda = 0.7$ , where  $\mu$  is the dynamic viscosity and  $\lambda$  is the thermal conductivity  
 of the gaseous phase).

### 3. Computational method and setup

210 SENGAP+, a three-dimensional compressible DNS code, is used for the present  
 numerical investigation, cf. e.g. [26, 27, 28]. It employs a tenth-order central  
 difference scheme for spatial discretisation for the internal grid points and the  
 order of differentiation decreases gradually to a one-sided second-order scheme  
 at the non-periodic boundaries. Explicit time advancement is implemented by a  
 215 low-storage third-order Runge-Kutta scheme [29] and the non-periodic boundary  
 conditions are specified via the Navier-Stokes Characteristic Boundary Condi-  
 tions (NSCBC) technique [30].

The canonical setup used for the present study is similar to several earlier DNS analyses on fuel spray combustion [31, 32, 33, 34, 35]. Here, a premixed and statistically planar stoichiometric n-heptane air flame is subjected to a constant water droplet stream from the inlet. Such a scenario can be imagined in both accidental explosions where the flame propagates towards a region below a water sprinkler system as well as in (advanced) internal combustion engines with separate fuel and water injection. A rectangular simulation domain of size  $30\delta_{th} \times 20\delta_{th} \times 20\delta_{th}$  has been considered for the present analysis, where the thermal flame thickness of the unstretched gaseous laminar (subscript  $L$ ) stoichiometric premixed flame is given by

$$\delta_{th} = \frac{T_{ad} - T_0}{\max |\nabla \hat{T}|_L}. \quad (8)$$

Note that the maximum flame temperature  $T_b$  usually remains below the adiabatic flame temperature  $T_{ad}$  because of the enthalpy sink associated with evaporating droplets. This domain is discretised using a Cartesian grid of size  $384 \times 256 \times 256$  points which ensures about 10 grid points within  $\delta_{th}$  and is also sufficiently fine to resolve the Kolmogorov length scale  $\eta$ . Partially non-reflecting boundary conditions are imposed in  $x$ -direction, i.e. the mean direction of flame propagation, while the  $y$ - and  $z$ -direction are considered to be periodic.

All simulations are allowed to evolve for at least four chemical time scales  $t_{chem} = D_0/S_L^2$ , with  $D_0$  being the unburned gas diffusivity, which corresponds to about three initial eddy turn-over times  $t_{turb} = L_{11}/u'$  for the turbulence intensity standard value of  $u'/S_L = 4$ . Hence, the simulation time of the current analysis is comparable to a number of recent DNS analyses, e.g. [27, 28, 33, 21].

To check upon their influence, key parameters defining the problem are varied in the following parametric analysis. Table 1 provides an overview of the different cases in terms of the turbulence intensity  $u'/S_L$ , normalized droplet diameter  $a_d/\delta_{th}$ , water mass fraction  $Y_W$  and latent heat of vaporization  $L_v$  of the water droplets. In this context, the laminar burning velocity  $S_L$  and the thermal flame thickness  $\delta_{th}$  refer to the purely gaseous laminar premixed stoichiometric n-heptane air flame without water droplets.

The normalized r.m.s. velocity fluctuation of  $u'/S_L = 4$  is sufficiently different from laminar conditions ( $u'/S_L = 0$ ) to examine the role of turbulence (mainly via flame wrinkling and turbulent mixing) but also sufficiently low to  
 250 exclude additional complexities due to flame stretch effects (relating to strain and curvature) which complicates the interpretation of the results at higher turbulence intensities. Following a Batchelor-Townsend energy spectrum, homogeneous isotropic velocity fluctuations are obtained from a standard pseudo-spectral method [36] and superimposed on the steady laminar premixed flame  
 255 solution to generate the initial condition. The normalized longitudinal integral length scale of turbulence is specified to be  $L_{11}/\delta_{th} = 2.5$ , i.e. the large-scale integral eddies are contained eightfold in the span-wise directions. Turbulence at the inlet is imposed consistently for these parameters.

The normalized droplet diameters of  $a_d/\delta_{th} = 0.02, 0.04$  and  $0.06$  correspond  
 260 to a range between 10 and 30  $\mu\text{m}$  in dimensional terms and are thus comparable to earlier experimental studies [11, 7, 2]. These mono-disperse droplets are initially distributed uniformly in space throughout the  $y$ - and  $z$ -direction on the unburned side of the flame, i.e. up to  $x/\delta_{th} \approx 10$ . Additionally, droplets are continuously injected at the inlet boundary such that a constant water mass  
 265 flux enters the domain. The ratio of the droplet to computational cell volume is  $V_d/\Delta V \approx 0.007, 0.057$  and  $0.191$  for  $a_d/\delta_{th} = 0.02, 0.04$  and  $0.06$ , respectively, thus justifying the sub-grid point source treatment of the evaporating droplets. The ratio of droplet diameters to the Kolmogorov length scale is  $a_d/\eta \approx 0.1, 0.2$  and  $0.3$  for  $a_d/\delta_{th} = 0.02, 0.04$  and  $0.06$ , respectively, for the highest turbulence  
 270 intensity of  $u'/S_L = 8$  investigated here. Both these ratios are comparable to several previous DNS analyses, e.g. [37, 38, 33, 21].

The quantity  $Y_W$  accounts for the water mass fraction in both phases, i.e.  $Y_W = Y_W^l + Y_W^g = m_W/(m_0 + m_W)$  where  $m_0$  is the initial unburned gas mass in the system before adding the liquid water droplets of mass  $m_W$ . This quantity  
 275 is independent of the product water generated by the chemical reaction. The normalized water loading  $m_W/m_0 = Y_W/(1 - Y_W)$  is also used in experiments to quantify the amount of water added to the system. The investigated values

$u'/S_L$	$a_d/\delta_{th}$	$Y_W$	$L_v$	Comment
4	-	0.0	-	gaseous premixed reference case
8	-	0.0	-	gaseous premixed reference case
4	0.04	0.1	$L_v^{\text{ref}}$	droplet reference case
4	0.06	0.1	$L_v^{\text{ref}}$	droplet size variation
4	0.02	0.1	$L_v^{\text{ref}}$	droplet size variation
4	0.04	0.05	$L_v^{\text{ref}}$	water loading variation
4	0.04	0.2	$L_v^{\text{ref}}$	water loading variation
0	0.04	0.1	$L_v^{\text{ref}}$	turbulence intensity variation
8	0.04	0.1	$L_v^{\text{ref}}$	turbulence intensity variation
4	0.04	0.1	$L_v^{\text{ref}}/2$	latent heat variation
4	0.04	0.1	$L_v^{\text{ref}}/4$	latent heat variation
4	0.04	0.1	$L_v^{\text{ref}}/8$	latent heat variation

Table 1: Case overview in terms of turbulence intensity  $u'/S_L$ , normalized droplet diameter  $a_d/\delta_{th}$ , water mass fraction  $Y_W = m_W/(m_0 + m_W)$  and latent heat of vaporization  $L_v$ ;  $L_v^{\text{ref}} = 2258$  kJ/kg is the latent heat of vaporization of water at boiling temperature.

of  $Y_W = 0.05, 0.1$  and  $0.2$  lie in the technically relevant range and are also comparable to earlier experimental studies [5, 10, 1].

280 The variation of  $L_v$  can be seen as numerical experiments to demonstrate the existence of different regimes of droplet flame interaction which are unlikely to be reached with the realistic fluid properties of liquid water. This behaviour is particularly controlled by the latent heat of vaporization which might be altered by additives in technical applications. The corresponding value of water  
285 droplets ( $L_v^{\text{ref}} = 2258$  kJ/kg) is the highest of all liquids and around seven times higher than the value of n-heptane fuel droplets ( $L_v = 315$  kJ/kg).

It is possible to define two dimensions spanning a regime diagram when complementing the above introduced quantities by the evaporation time scale  $\tau_v$ , the flame time scale  $\tau_f$  (detailed in Sec. 4.4) and the mean separation distance

290 between droplets,

$$\delta_s = \sqrt[3]{\frac{V_0}{N_d}}, \quad (9)$$

where  $V_0$  is the volume of the unburned part of the domain occupied by  $N_d$  droplets. The ratio of evaporation and flame time scales  $\tau_v/\tau_f$ , also known as the evaporation Damköhler number in spray combustion (fuel instead of water droplets) and the ratio of the mean distance between droplets and the flame  
295 thickness  $\delta_s/\delta_f$  together allow for different regimes of droplet flame interaction to be distinguished:

1. “reduced enthalpy” regime characterized by slow evaporation ( $\tau_v \gg \tau_f$ ) and high droplet density ( $\delta_s \ll \delta_f$ ), top left panel in Fig. 1;
2. “ineffective” regime characterized by slow evaporation ( $\tau_v \gg \tau_f$ ) and low  
300 droplet density ( $\delta_s \gg \delta_f$ ), top right panel in Fig. 1;
3. “effective attenuation” regime characterized by fast evaporation ( $\tau_v \ll \tau_f$ ) and high droplet density ( $\delta_s \ll \delta_f$ ), bottom left panel in Fig. 1;
4. “inhomogeneously perturbed” regime characterized by fast evaporation ( $\tau_v \ll \tau_f$ ) and low droplet density ( $\delta_s \gg \delta_f$ ), bottom right panel in  
305 Fig. 1.

The names given to the different regimes aim to reflect the dominant mechanism. Further research, i.e. scaling considerations or a larger number of simulations, is necessary to establish the location of the boundaries between different regimes, which represent smooth transition regions rather than abrupt changes  
310 of behaviour. Turbulence intensity is conceivable as a third dimension of the diagram since it could be responsible for the shifting of regime boundaries, e.g. via the influence of turbulent mixing.

For the conditional evaluation of statistics, it is convenient to define a unique mapping within the flame by means of a reaction progress variable (oxygen-  
315 based here):

$$c = \frac{Y_{O,0} - Y_O}{Y_{O,0} - Y_{O,b}}, \quad (10)$$

which essentially compares the local mass fraction  $Y_O$  with the pre-flame composition  $Y_{O,0}$  (corresponding to  $c = 0$ ) and the chemical equilibrium  $Y_{O,b}$  (cor-

responding to  $c = 1$ ). In this way, iso-contours of  $c$  can be used to indicate the extent of the flame as in Fig. 1.

320 Depending on the regime, different consequences on key flame characteristics such as flame surface area  $A$ , unstrained laminar burning velocity  $S_L$  and maximum flame temperature  $T_b$  can be expected. The latter two quantities are directly linked as further discussed in Sec. 4.4. The least influence on the flame is expected in regime (ii) where both the cooling and dilution effects are small.

325 In regime (i), the cooling effect is dominant, leading to a non-negligible reduction of both burning velocity and flame temperature. However, the evaporation of droplets, and therefore the reduction of exhaust gas temperature, continues in the post-flame region which can be important in the context of emissions prediction, particularly relating to the temperature-sensitive production rate of

330  $\text{NO}_x$ . A significant effect on burning velocity and flame temperature is to be expected in regime (iii). Despite the fast evaporation, the water vapour is rather homogeneously distributed within the flame due to the densely packed droplets, unlike in regime (iv). Regime (iv) is the only one in which a non-negligible influence on the flame surface area must be expected. Here, it is important to

335 mention that the size of the water droplets in relation to the thickness of the flame is not to the scale in Fig. 1. The investigated droplets are actually between one and two orders of magnitude smaller than the flame thickness. Hence, it is not the droplets itself but the effective vapour cloud around them which leads to additional wrinkling of the flame besides turbulence. Depending on the

340 scenario, this can be either beneficial, e.g. in internal combustion engines, or detrimental, e.g. in accidental explosions, as it affects the overall burning rate represented by the effective turbulent burning velocity  $S_T$ .

## 4. Results and discussion

### 4.1. Cooling and dilution effects on key flame characteristics

345 The free parameters of water addition, which are the droplet size  $a_d/\delta_{th}$  and water loading  $Y_W$ , are varied in all of the following evaluations.

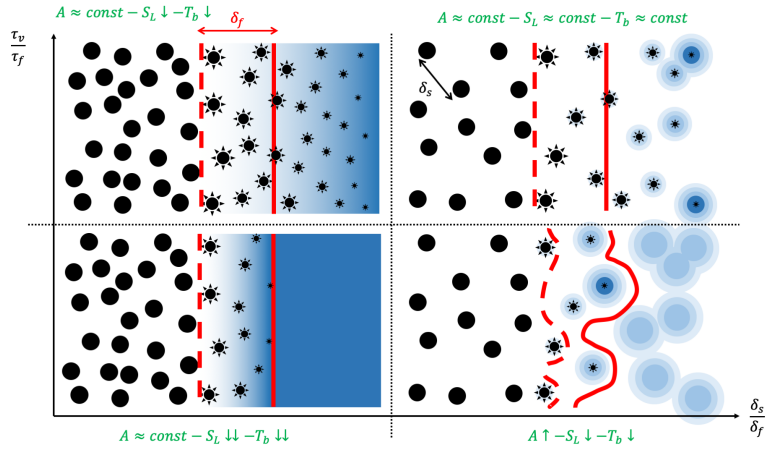


Figure 1: Schematic regime diagram of water droplet flame interaction. Separated by a mean distance of  $\delta_s$ , liquid water droplets are represented by black objects and the amount of gaseous water, i.e. steam, is indicated by the intensity of the blue colour. The dashed red line ( $c = 0$ ) and the continuous red line ( $c = 1$ ) are supposed to locate the flame of thickness  $\delta_f$  between the unburned and burned mixture.  $\tau_v$  and  $\tau_f$  denote the evaporation and flame time scale, respectively. Expected trends of key flame characteristics, such as flame surface area  $A$ , laminar burning velocity  $S_L$  and maximum flame temperature  $T_b$ , are stated in a green coloured font.

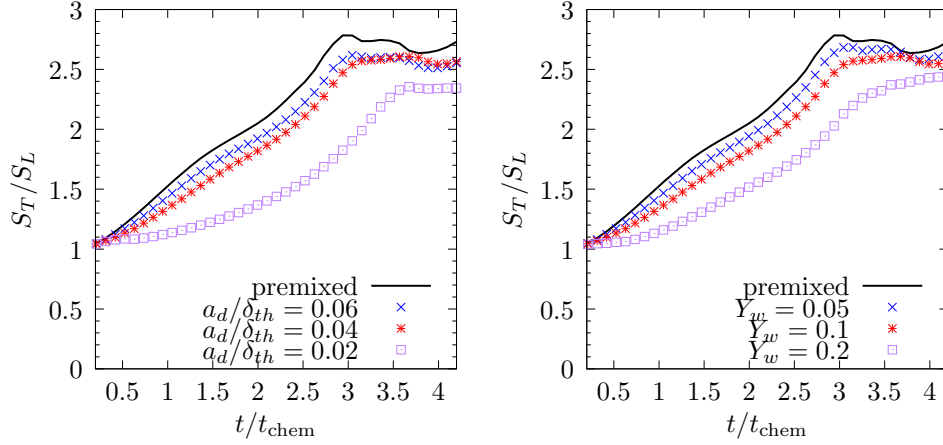


Figure 2: Turbulent flame speed  $S_T$ , normalized by the unstretched laminar burning velocity  $S_L$  of the stoichiometric premixed flame, depending on the initial droplet size  $a_d/\delta_{th}$  (left) and water loading  $Y_W$  (right).

The first quantity of major interest is the turbulent burning velocity

$$S_T = \frac{\int_V \dot{\omega}_F dV}{\rho_0 A_\perp (Y_{F,0} - Y_{F,b})} \quad (11)$$

as shown in Fig. 2, where  $\rho_0$ ,  $A_\perp$ ,  $Y_{F,0}$  and  $Y_{F,b}$  are the unburned gas density, projected flame area in the direction of mean flame propagation, fuel mass fraction in the unburned and fully burned gases in the unstretched stoichiometric gaseous premixed flame, respectively. If not explicitly stated otherwise, the initial r.m.s. velocity fluctuation should be understood to be  $u'/S_L = 4$  in all of the turbulent cases considered. Decreasing  $a_d/\delta_{th}$  or increasing  $Y_W$  results in a clear attenuation of  $S_T$  as it is evident from the comparison of the black line representing the premixed case with the symbols representing the droplet cases in Fig. 2.

Figures 3 and 4 show two different measures of flame surface area by volume integration of the surface density function, i.e.

$$A(c) = \int_V |\nabla c| dV \quad (12)$$

and

$$A(T) = \int_V |\nabla T| dV, \quad (13)$$

360 based on the reaction progress variable  $c$  and normalized temperature  $T$ , respectively. The results from both definitions are identical for purely gaseous premixed combustion at unity Lewis number (represented by the black lines in Figs. 3 and 4), where  $c = T$  holds, but this is clearly not the case under the influence of droplets (represented by symbols of the same kind in Figs. 3 and
 365 4). **Alternative definitions of flame surface area based on the fine-grained flame surface density, i.e. based on non-unique iso-surfaces  $c = c^*$ , have been shown to be generally less robust for arbitrary regimes of combustion [16] and are therefore not used in the present study.** Inspecting  $A(c)$ , which is based on oxygen concentration according to Eq. 10, the droplets lead to a consistent decrease
 370 of  $A(c)$  compared to the purely gaseous premixed flame. As elaborated in Sec. 4.2, the reason for this behaviour is connected to the dampening influence of the evaporating droplets on the turbulent flow field. The turbulence is mainly responsible for the wrinkling of the flame and therefore the general increase of flame surface area over the time period investigated. In contrast, the droplets
 375 can even lead to an increase of  $A(T)$ , which is based on normalized temperature, and to non-monotonic behaviour in terms of droplet size in the time range  $3 < t/t_{\text{chem}} < 4$ . The three-dimensional visualization of  $c = 0.95$  and  $T = 0.95$  iso-contours shown in Fig. 5, taken shortly after the first droplets have penetrated through the flame, reveals that the slowly evaporating water droplets
 380 lead to insignificant steam release (i.e. minimal changes of local mixture composition and thus  $A(c)$ ) within the flame but to considerable small-scale wrinkling of the temperature field (i.e. local dimples increasing  $A(T)$ ) due to the enthalpy sink associated with them. This comparison suggests that the cooling effect outweighs the dilution effect of liquid water droplets interacting with premixed
 385 flames. **Figure 6 shows the average steam mass fraction  $Y_W^g$  (product water excluded) in the flame region ( $0.01 < c < 0.99$ ) for the droplet reference case (initial  $u'/S_L = 4$ ,  $a_d/\delta_{th} = 0.04$ ,  $Y_W = 0.1$ ) and for the small droplets (initial  $u'/S_L = 4$ ,  $a_d/\delta_{th} = 0.02$ ,  $Y_W = 0.1$ ). Even for the small droplets that are evaporating the fastest, the steam mass fraction remains below 4% within the
 390 flame which is clearly below the overall water loading of  $Y_W = Y_W^g + Y_W^l = 0.1$ .**

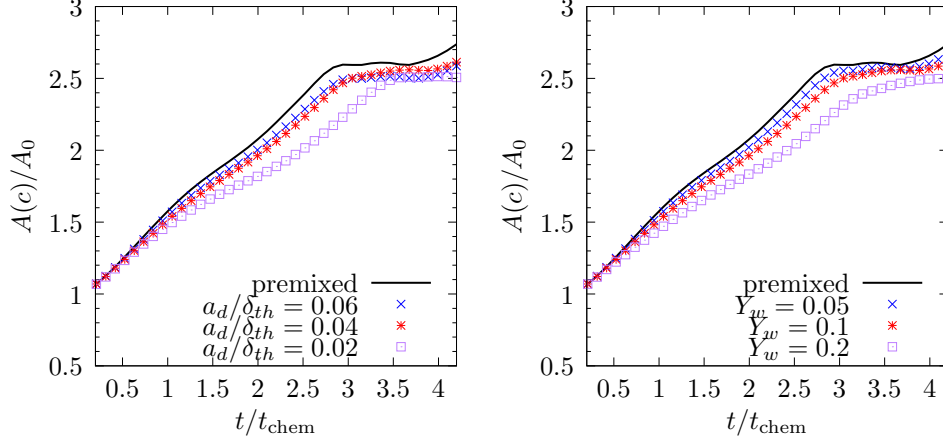


Figure 3: Species concentration based flame surface area  $A(c)$ , normalized by the projected flame area in the direction of mean flame propagation  $A_{\perp}$  (which is also the initial flame surface area for the planar flame  $A_0$ ), depending on the initial droplet size  $a_d/\delta_{th}$  (left) and water loading  $Y_w$  (right).

Hence, it is assumed that the chemical effect due to water addition (which is neglected in this work) is small due to the small added steam concentrations within the flame. These observations hold for at least the parameter range considered and when using realistic fluid properties of water. The effects of varying the volatility of the liquid droplets are described in Sec. 4.3.

The evolution of turbulent burning velocity  $S_T$  and flame surface area  $A$  are strongly linked as confirmed by the above evaluations. To isolate the different effects of droplet flame interaction, it is useful to examine the amount of burning per unit area of flame,

$$\Omega = \frac{\int_V \dot{\omega}_c dV}{\int_V |\nabla c| dV}. \quad (14)$$

Deviations of the ratio

$$\frac{S_T/S_L}{A/A_{\perp}} = \frac{\Omega}{\rho_0 S_L} \quad (15)$$

from unity can be used to quantify the departure from the idealised behaviour as postulated in Damköhler's first hypothesis. Note that  $S_T = \int_V \dot{\omega}_c dV / (\rho_0 A_{\perp})$  and the flame area projected on the direction of mean flame propagation  $A_{\perp}$  is identical to the initial flame surface area  $A_0$  for the statistically planar flame.

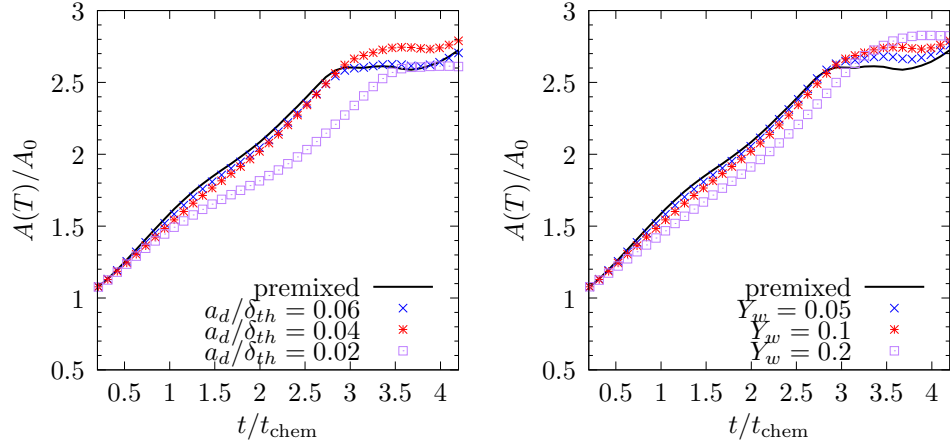


Figure 4: Temperature based flame surface area  $A(T)$ , normalized by the projected flame area in the direction of mean flame propagation  $A_{\perp}$  (which is also the initial flame surface area for the planar flame  $A_0$ ), depending on the initial droplet size  $a_d/\delta_{th}$  (left) and water loading  $Y_W$  (right).

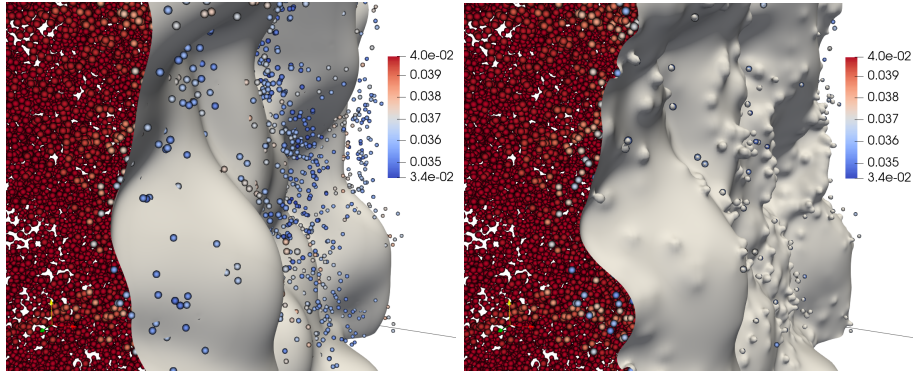


Figure 5: Instantaneous realization of the droplet reference case (initial  $u'/S_L = 4$ ,  $a_d/\delta_{th} = 0.04$ ,  $Y_W = 0.1$ ): Three-dimensional gray iso-contours of  $c = 0.95$  (left) and  $T = 0.95$  (right) at  $t/t_{chem} = 1.1$ . The colour of the not-to-the-scale droplets indicates the instantaneous normalized droplet diameter  $a_d/\delta_{th}$ .

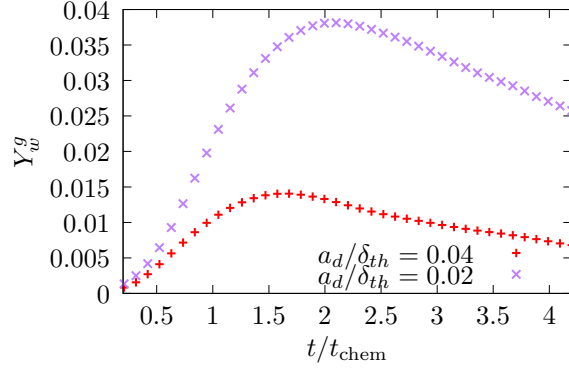


Figure 6: Average steam mass fraction  $Y_W^g$  (product water excluded) in the flame region ( $0.01 < c < 0.99$ ) for the droplet reference case (initial  $u'/S_L = 4$ ,  $a_d/\delta_{th} = 0.04$ ,  $Y_W = 0.1$ ) and for the small droplets (initial  $u'/S_L = 4$ ,  $a_d/\delta_{th} = 0.02$ ,  $Y_W = 0.1$ ).

405 The results shown in Fig. 7 indicate a maximum reduction of  $\Omega$  of about 30% for the smallest droplets considered (purple symbols representing droplets of initial size  $a_d/\delta_{th} = 0.02$ ) compared to the purely gaseous premixed case (represented by the black line). The reduction effect apparently decreases considerably over the simulated time period and possible explanations are discussed in Sec. 4.2, 410 which focuses on the intricate role of turbulence. To demonstrate the behaviour of  $\Omega$  with respect to droplet size  $a_d/\delta_{th}$  and overall water loading  $Y_W$ , horizontal lines in Fig. 7 indicate a hypothetical linear scaling. The minimum value of  $\Omega$  for the droplet reference case (initial  $u'/S_L = 4$ ,  $a_d/\delta_{th} = 0.04$ ,  $Y_W = 0.1$ ) is used as a base for the comparison. As might be expected, the water loading shows a 415 fairly linear influence, whereas the droplet size shows a non-linear influence due to its quadratic influence on the law governing evaporation (cf. Eq. 18).

Another quantity of key interest is the flame thickness. Figure 8 presents the temporal evolution of the mean thickness defined as

$$\delta_f = \frac{V_{0.1 < c < 0.9}}{\int_V |\nabla c| dV} \quad (16)$$

in relation to the thermal flame thickness  $\delta_{th}$  of the unstretched laminar stoichiometric premixed flame. The trends of flame thickness are opposite to the 420 trends of  $\Omega$  which can already be understood by analogy to the definition of

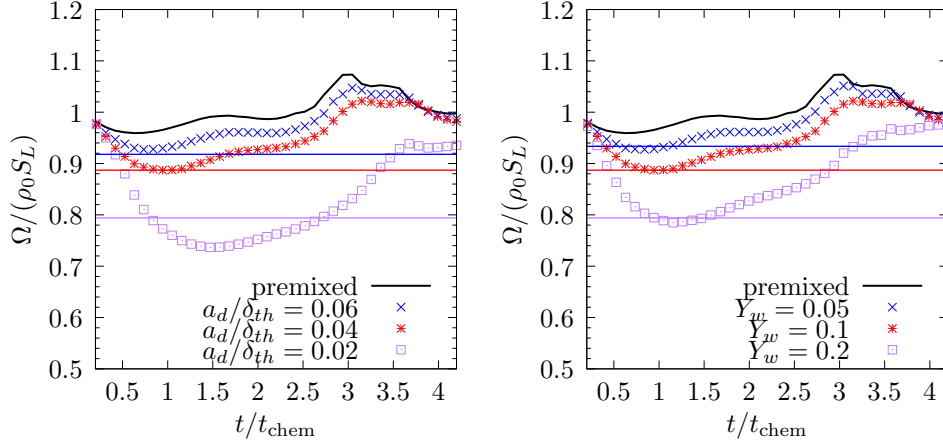


Figure 7: Normalized amount of burning per unit area of flame  $\Omega/(\rho_0 S_L)$ , depending on the initial droplet size  $a_d/\delta_{th}$  (left) and water loading  $Y_W$  (right); **Horizontal green lines indicate a hypothetical linear scaling using the droplet reference case (initial  $u'/S_L = 4$ ,  $a_d/\delta_{th} = 0.04$ ,  $Y_W = 0.1$ ) as a base for comparison.**

the Zel'dovich flame thickness  $\delta_Z = D_0/S_L$ . The somewhat arbitrary threshold values ( $0.1 < c < 0.9$ ) for flame volume calculation are adequate for the comparison of the relative influences of  $a_d$  and  $Y_W$ . Nevertheless, an alternative view on flame thickness is presented in Fig. 9 based on the surface density function  $|\nabla c|$  [39, 22] conditional on reaction progress variable  $c$  for a particular point in time. Considering the definition of the thermal flame thickness (Eq. 8), it is not surprising that the maximum value of the normalized equivalent quantity  $|\nabla c|\delta_{th}$  is close to unity for the purely gaseous premixed reference case (represented by the black line in Fig. 9) and consequently lower for the thicker flames that are affected by droplets (represented by symbols in Fig. 9). The maximum of  $|\nabla c|$  is found at  $c \approx 0.6$  in all cases. It is also worth noting that the surface density function is closely related to the scalar dissipation rate  $D_c|\nabla c|^2$  [40] and generalized flame surface density  $\Sigma_{gen} = \langle |\nabla c| \rangle$  [41], where  $\langle \cdot \rangle$  indicates an appropriate averaging/filtering operation. These quantities are of central importance to the associated modelling concepts. It can be concluded that the results of different flame thickness definitions are generally consistent

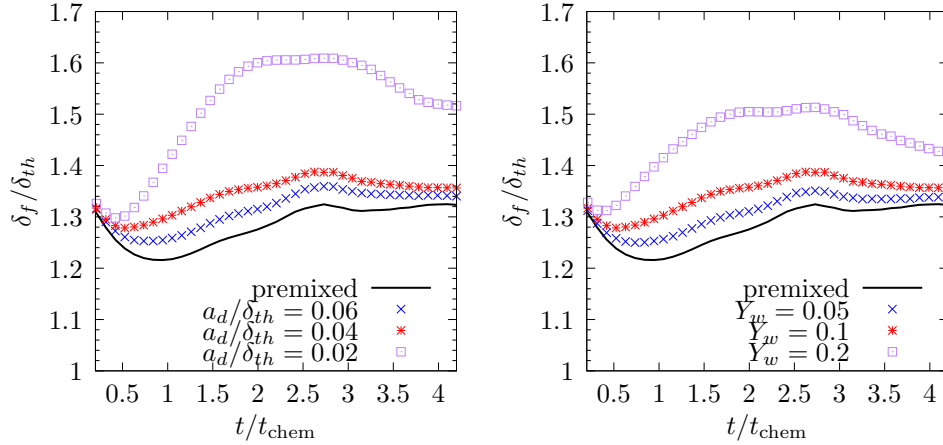


Figure 8: Mean flame thickness  $\delta_f$ , normalized by the thermal flame thickness  $\delta_{th}$  of the unstretched laminar stoichiometric premixed flame, depending on the initial droplet size  $a_d/\delta_{th}$  (left) and water loading  $Y_w$  (right).

and both views complement each other: the transient nature of the interaction is reflected by the evolution of  $\delta_f$  (Fig. 8), whereas additional information can  
 440 be extracted from the conditional surface density function (Fig. 9).

Since the burning velocity is strongly affected by the temperature distribution within the flame, it is worthwhile to examine the probability density function of the normalized temperature  $T$  in the flame region ( $0.01 < c < 0.99$ ), as shown by Fig. 10. Compared to the gaseous premixed reference case (black  
 445 line in Fig. 10), the droplet case PDFs (blue, red and purple lines in Fig. 10) are wider and their maximum on the burned gas side is shifted to smaller values of  $T$ . In this way, the cooling effect within the flame due to droplet evaporation can be quantified. Mainly depending on their size, the evaporation of droplets and reduction of exhaust gas temperature continue in the post-flame  
 450 region. It is also important in globally unsteady flame propagation, like accidental explosions, where the thermal expansion of the burned gases is a major driver determining the overall velocity of flame propagation. Hence, the stream-wise variation of the span-wise averaged normalized temperature  $\bar{T}$  is shown in Fig. 11 for the given parameter range. The maximum normalized temperature

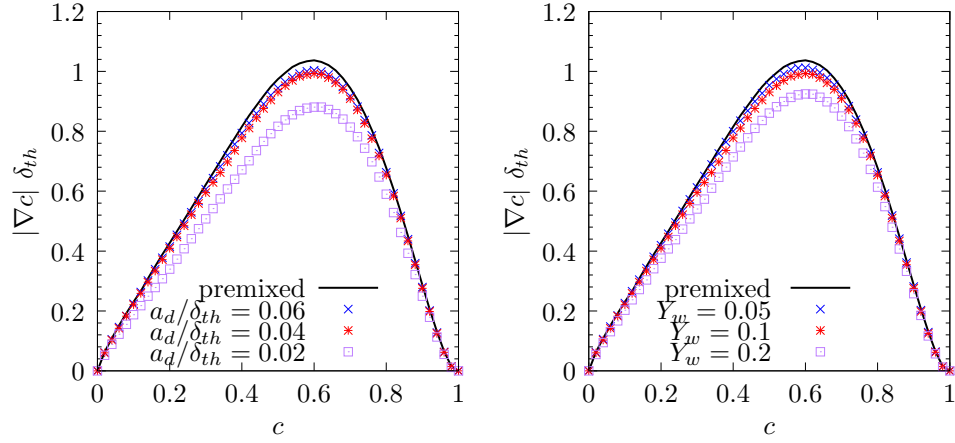


Figure 9: Surface density function  $|\nabla c|$ , normalized by the thermal flame thickness  $\delta_{th}$  of the unstretched laminar stoichiometric premixed flame, conditional on reaction progress  $c$  at  $t/t_{chem} = 3$ , depending on the initial droplet size  $a_d/\delta_{th}$  (left) and water loading  $Y_W$  (right).

455 within the flame, i.e. where the kink in the averaged temperature profile appears (best visible for the smallest droplets of initial size  $a_d/\delta_{th} = 0.02$ , represented by purple symbols in Fig. 11, at  $x/\delta_{th} \approx 20$ ), is denoted as  $T_b$  in the following and the observed values are in agreement with the peaks of the PDFs of  $T$  on the burned gas side in Fig. 10. The computational domain is not long enough to  
 460 observe the final steady-state temperature after full evaporation of all droplets. A reduced-order modelling strategy for a-priori predictions of  $T_b$  in the presence of water droplets is developed in Sec. 4.4.

#### 4.2. Role of turbulence

The droplets and the turbulence are coupled to each other in a non-trivial  
 465 way. The droplets are not only transported by the turbulent flow but also have an effect on it as well as on the flame. A related phenomenon is called turbophoresis [42, 43] and describes the tendency for particles or droplets to migrate in the direction of decreasing local turbulence level. Once the initially homogeneous turbulence field and the flame start to adapt to each other, a  
 470 non-homogeneous turbulence field evolves. Due to their relatively small Stokes

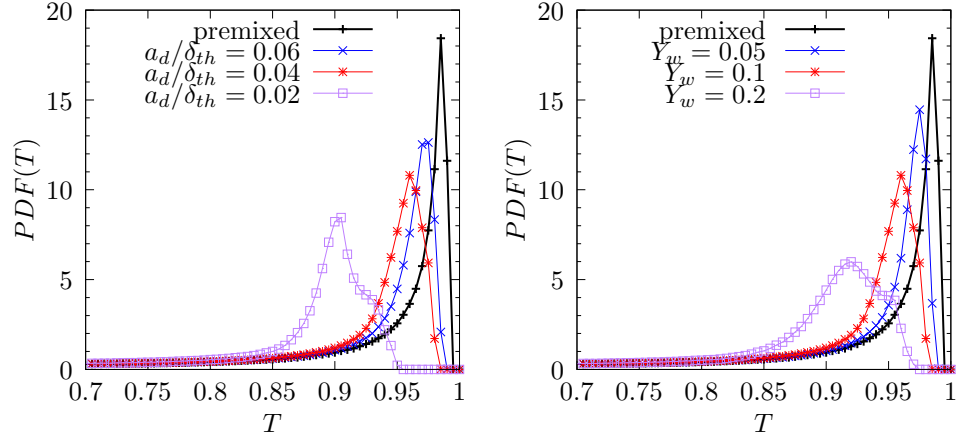


Figure 10: PDFs of the normalized temperature  $T$  in the flame region ( $0.01 < c < 0.99$ , but only the burned gas side is shown here) at  $t/t_{\text{chem}} = 3$ , depending on the initial droplet size  $a_d/\delta_{th}$  (left) and water loading  $Y_w$  (right).

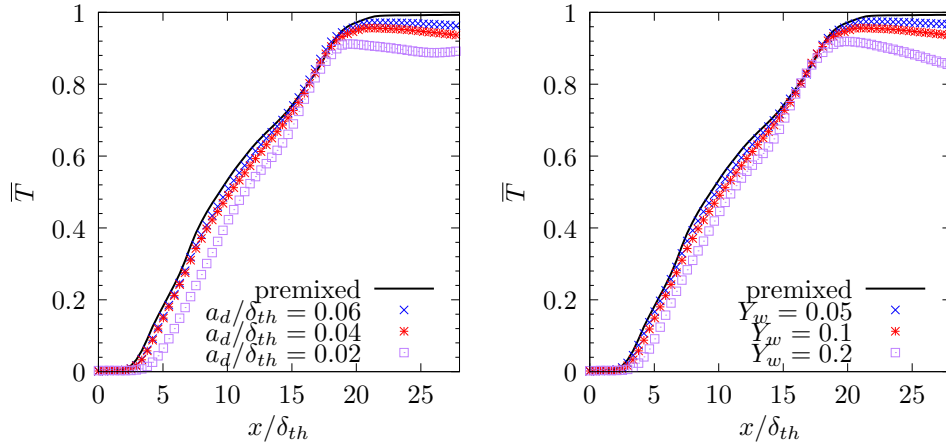


Figure 11: Variation of the span-wise averaged normalized temperature  $\bar{T}$  in mean flow direction  $x$  at  $t/t_{\text{chem}} = 4$ , depending on the initial droplet size  $a_d/\delta_{th}$  (left) and water loading  $Y_w$  (right).

number (ratio of particle relaxation time scale to characteristic time scale of the flow), the water droplets investigated here mostly follow the turbulent fluid motion. Nevertheless, particle/droplet clustering [44, 45] occurs as demonstrated by the comparison of the solution for two different points in time shown in Fig. 12. At an early stage ( $t/t_{\text{chem}} = 1.6$ ; top panels in Fig. 12), the droplets represented by not-to-the-scale black dots are still rather homogeneously distributed, whereas appreciable clustering can be discerned at a later stage of the simulation ( $t/t_{\text{chem}} = 4.1$ ; bottom panels in Fig. 12) in the unburned part of the domain, i.e. where  $T \approx 0$ . Compared to non-clustered particles, coherent clusters show a stronger tendency to occur in regions of high strain and low vorticity according to Baker et al. [46]. The impact of droplets on the overall burning rate considerably decreases between these two points in time as indicated by the evolution of  $\Omega$  in Fig. 7 (note the discrepancy between the black line representing the premixed case and the symbols representing the droplet cases). The transient nature of the problem and the uniformity of droplet distribution in the fresh gas facing the flame may be factors related to this observation. Also note the localized enthalpy defects (characterized by local occurrences of  $T < 1$  in the hot exhaust gas) as well as the inhomogeneous distribution of  $Y_W^g$  (product water excluded) due to the localized steam release at the location of the evaporating droplets which can be clearly recognized in Fig. 12.

To elaborate further on the role of turbulence, the spatial variation of the r.m.s. velocity fluctuation  $u' = \sqrt{2k/3}$  with stream-wise distance is depicted in Fig. 13, where the turbulent kinetic energy is given by

$$k = \frac{1}{2} \left( \overline{u'_1 u'_1} + \overline{u'_2 u'_2} + \overline{u'_3 u'_3} \right). \quad (17)$$

It is generally known that homogeneous isotropic turbulence, as imposed at the domain inlet, decays monotonically in space. In contrast, Fig. 13 shows a non-monotonic decrease of turbulence intensity with stream-wise distance. Since the flame constitutes the only element different to the idealized scenario of decaying turbulence, the local increase of  $u'$  and therefore globally non-monotonic decay, must be due to the flame. To indicate the strong correlation between

500 the turbulent flame brush, characterized by  $\partial\bar{c}/\partial x > 0$ , and the local increase  
 of  $u'$ , the spatial distributions of the span-wise averaged reaction progress vari-  
 able  $\bar{c}$  are presented in Fig. 13 as continuous lines. This general trend is the  
 same for all cases but the local increase of  $u'$  around the mean position of the  
 flame ( $x/\delta_{th} \approx 13$ ), which is generated by the flame itself, shows clear differ-  
 505 ences. One might assume that the cooling effect of droplets (corresponding cases  
 represented by coloured symbols in Fig. 13) leads to lower kinematic viscosities  
 compared to the purely gaseous premixed reference flame (black symbols in Fig.  
 13), and thus higher turbulence intensities, but this is apparently not a domi-  
 nant effect here. Instead, the local peak due to flame-generated turbulence is  
 510 attenuated depending on the droplet size and water loading. It is known from  
 numerical [47, 48, 49] and experimental [50] studies that the relative strength of  
 flame-generated turbulence depends on the strength of heat release (determined  
 by density ratio, turbulence intensity and characteristic Lewis number). The  
 density ratio drops via the local release of steam and the cooling effect (Fig. 10)  
 515 of water droplets which explains the significant reduction of flame-generated  
 turbulence and subsequently wrinkling of the flame (Fig. 3). The smaller the  
 initial droplet size or the higher the water loading, the stronger this dampening  
 effect becomes as it is evident from the comparison of the droplet cases repre-  
 sented by coloured symbols with the premixed case represented by the black  
 520 symbols in Fig. 13.

Additional observations on the influence of turbulence intensity are facili-  
 tated by Fig. 14 which shows the temporal evolution of  $\Omega$  (Eq. 14) and the  
 PDFs of  $T$  in the flame region ( $0.01 < c < 0.99$ ) for varying turbulence inten-  
 sity  $u'/S_L$  as indicated by the different colours. In terms of droplet parameters,  
 525 only the standard values, i.e.  $a_d/\delta_{th} = 0.04$  and  $Y_W = 0.1$ , are utilized here.  
 For the highest value of turbulence intensity (initial  $u'/S_L = 8$ ; purple colour),  
 the amount of burning per unit area of flame  $\Omega$  is highly irregular over time,  
 partly due to additional phenomena like flame stretch effects (which are not at  
 the focus of this work). Apart from very few exceptions, the  $\Omega$  values of the  
 530 droplet cases (represented by symbols in Fig. 14) are consistently lower than of

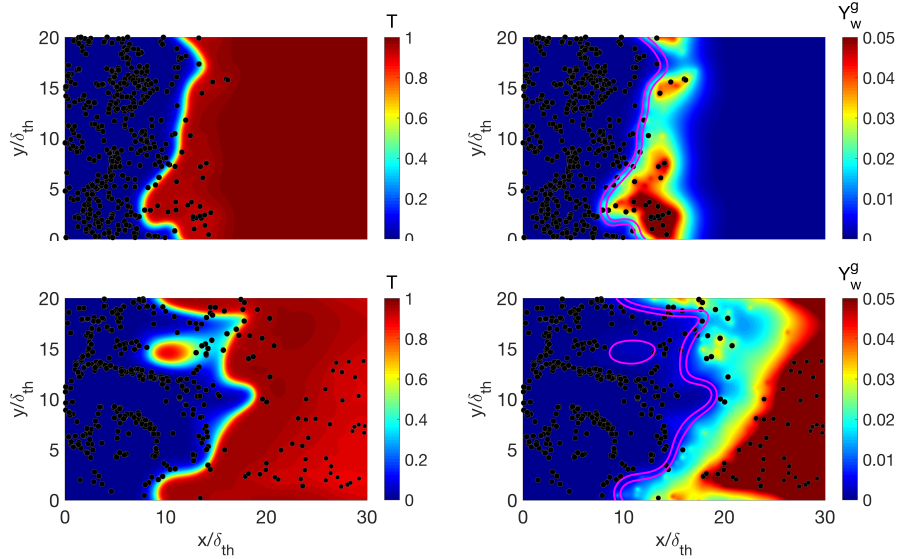


Figure 12: Instantaneous realizations of the droplet reference case (initial  $u'/S_L = 4$ ,  $a_d/\delta_{th} = 0.04$ ,  $Y_W = 0.1$ ): Mid-plane slices of normalized temperature  $T$  (left panels) and steam mass fraction  $Y_W^g$  (product water excluded; right panels) at  $t/t_{\text{chem}} = 1.6$  (top panels) and  $t/t_{\text{chem}} = 4.1$  (bottom panels). The magenta lines correspond to  $c = 0.5$  and  $c = 0.9$ , respectively. Black dots representing the droplets are not to the scale.

the corresponding purely gaseous premixed cases (represented by lines in Fig. 14) at the same initial turbulence intensity (i.e. same colour). This discrepancy is most clear for the laminar case ( $u'/S_L = 0$ ; blue colour), where  $\Omega = \rho_0 S_L$  holds in the absence of water droplets, and this is masked increasingly by elevated turbulence intensities. A comparison of the PDFs of  $T$  in Fig. 14, as used

535 vated turbulence intensities. This discrepancy is most clear for the laminar case ( $u'/S_L = 0$ ; blue colour), where  $\Omega = \rho_0 S_L$  holds in the absence of water droplets, and this is masked increasingly by elevated turbulence intensities. A comparison of the PDFs of  $T$  in Fig. 14, as used previously to quantify the cooling effect, reveals that turbulent mixing of the local enthalpy defects in the vicinity of the droplets leads to a somewhat wider probability distribution of temperature values within the flame.

### 4.3. Volatility of water

540 Water is characterized by the highest specific heat and latent heat of vaporization of all liquids as well as a very high gas-liquid density ratio. This avoids significant pre-evaporation ahead of the flame and ensures that mainly the hot

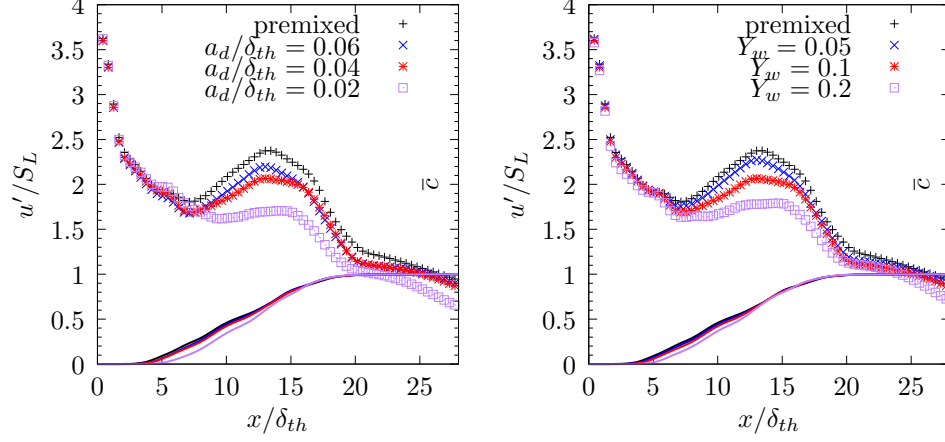


Figure 13: Variation of the r.m.s. velocity fluctuation  $u'$  (symbols), normalized by the unstretched laminar burning velocity  $S_L$  of the stoichiometric premixed flame, and span-wise averaged reaction progress variable  $\bar{c}$  (continuous lines) in mean flow direction  $x$  at  $t/t_{\text{chem}} = 3$ , depending on the initial droplet size  $a_d/\delta_{th}$  (left) and water loading  $Y_W$  (right).

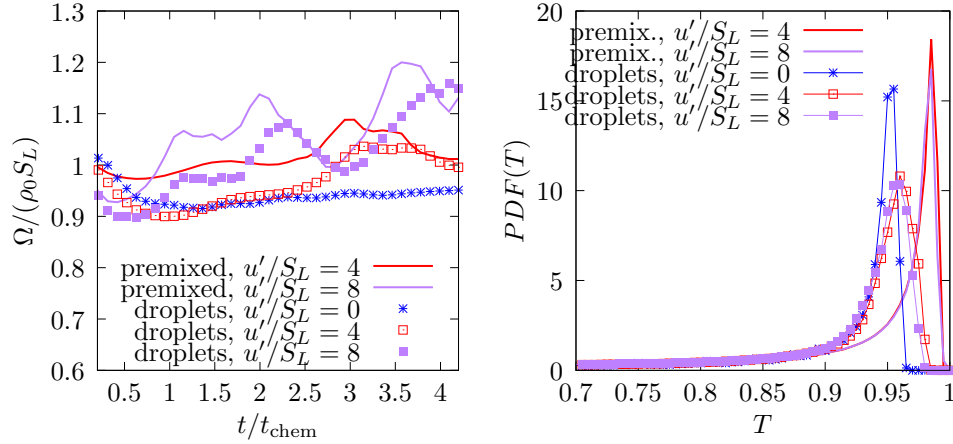


Figure 14: Normalized amount of burning per unit area of flame  $\Omega/(\rho_0 S_L)$  (left) and PDFs of the normalized temperature  $T$  (right) in the flame region ( $0.01 < c < 0.99$ , but only the burned gas side is shown here) at  $t/t_{\text{chem}} = 3$ , for different initial levels of r.m.s. velocity fluctuation  $u'$ , normalized by the unstretched laminar burning velocity  $S_L$  of the stoichiometric premixed flame;  $a_d/\delta_{th} = 0.04$  and  $Y_W = 0.1$  in all droplet cases.

exhaust gas is cooled. At the same time, the relatively slow evaporation allows only for a limited influence on the flame itself. These conditions are quite different to those encountered in the field of spray combustion, where fuel is initially  
545 supplied in the liquid phase. The liquid droplet properties of n-heptane and water are compared in Table 2.

Since the evaporation behaviour is strongly influenced by the latent heat of vaporization  $L_v$ , this quantity is varied here from the realistic value corresponding to water  $L_v^{\text{ref}}$  down to an eightfold smaller value of  $L_v^{\text{ref}}/8$  as a numerical  
550 experiment. The value  $L_v^{\text{ref}}/8$  is somewhat smaller than the realistic value corresponding to n-heptane. Inspecting the corresponding evolution of  $\Omega$  (Eq. 14) shown in Fig. 15, it can be assumed that the dilution effect becomes increasingly important in relation to the cooling effect when the latent heat is lowered. In  
555 these cases, a considerable amount of steam is released within the flame due to faster evaporation. Hence, in order to conserve mass, the mass fractions of oxidizer and fuel need to locally decrease and consequently the burning velocity decreases. Furthermore, the species concentration based flame surface area  $A(c)$  as shown in Fig. 15 is increased by about 50% for the smallest latent heat value  
560 ( $L_v^{\text{ref}}/8$ ; orange symbols) compared to the purely gaseous premixed reference case (black line), before this is increasingly compensated by the strong dampening effect of evaporating droplets on the flame-generated turbulence (cf. Sec. 4.2). It is assumed that the droplet-induced flame wrinkling occurs on a comparatively narrow range of length scales determined by the effective size of the  
565 vapour cloud surrounding the individual droplets (considerably larger than the size of the droplets itself), as opposed to the broad-band flame wrinkling due to turbulence. Relating to the regime classification as introduced earlier (Fig. 1), the most extreme case ( $L_v = L_v^{\text{ref}}/8$ ) can certainly be assigned to regime (iv), “inhomogeneously perturbed”, whereas the case with realistic fluid properties  
570 ( $L_v = L_v^{\text{ref}}$ ) can be assigned to either regime (i) or (ii), “reduced enthalpy” or “ineffective”, depending on how the boundary between both regimes is defined.

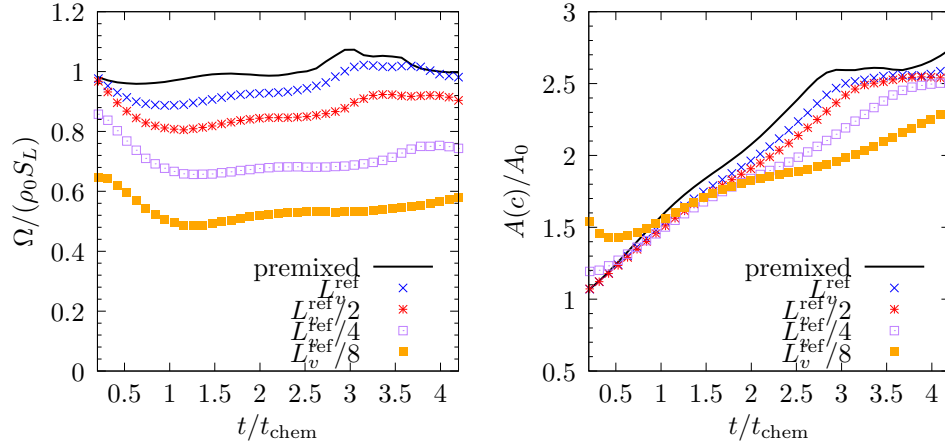


Figure 15: Normalized amount of burning per unit area of flame  $\Omega/(\rho_0 S_L)$  (left) and normalized flame surface area  $A(c)/A_0$  (right), depending on the latent heat of vaporization  $L_v$ ;  $a_d/\delta_{th} = 0.04$  and  $Y_W = 0.1$  in all droplet cases.

	n-heptane	water	Unit
Density	684.0	999.9	kg/m <sup>3</sup>
Molecular mass	100.0	18.02	g/mol
Latent heat of vaporization (at boiling temperature)	315.0	2258.0	kJ/kg
Specific heat at constant pressure	2296.45	4181.0	J/kg/K

Table 2: Comparison of liquid droplet properties of n-heptane and water.

#### 4.4. Reduced-order modelling

The purpose of this section is to devise a reduced-order model for the cooling and dilution effects of water droplets interacting with premixed (turbulent) flames, primarily to support the understanding of the complex droplet-flame interaction process. After additional fine-tuning with respect to the influence of turbulence (as discussed at the end of this section), the model can potentially replace the need for computationally expensive high-fidelity simulations. The model predictions can eventually be assessed by the DNS database established in this work.

Based on the observations from the parametric analysis, the central idea underlying the model is a comparison of the time scales representing evaporation and the flame. Only if the evaporation is sufficiently fast compared to the residence time within the flame, the droplet interaction is significantly affecting the flame structure. First of all, the evaporation time scale  $\tau_v$  can be devised from the well-known (diameter)<sup>2</sup>-law which assumes steady-state evaporation and constant fluid properties:

$$\tau_v = a_d^2 \left( \frac{8\lambda_g}{C_p^g \rho_d} \ln(1 + B_T) \right)^{-1} = a_d^2 / K_v, \quad (18)$$

where  $K_v$  is the evaporation constant. This relation can be extended for increased heat and mass transfer due to convective flow around the droplets, e.g. by incorporating the well-established correlation of Ranz and Marshall [51]:

$$\tau_v = a_d^2 \left( \frac{8\lambda_g}{C_p^g \rho_d} \ln(1 + B_T) \left( 1 + 0.3 \text{Re}_d^{1/2} \text{Pr}_g^{1/3} \right) \right)^{-1}, \quad (19)$$

where  $\text{Re}_d = |\vec{u}(\vec{x}_d, t) - \vec{u}_d| a_d / \nu = u_{\text{rel}} a_d / \nu$  is based on the relative velocity  $u_{\text{rel}}$  between both phases. In the absence of prior information about the flow, it may be justified in some cases to calculate the droplet Reynolds number as  $\text{Re}_d = u' a_d / \nu$  using the imposed turbulence intensity, but this is discarded here because of the small Stokes number of the droplets. Nevertheless, it is worth mentioning this possibility since it provides a link between  $u'$  and  $\tau_v$  which can be useful for future scaling considerations on the role of turbulent mixing. Equation 19

seems to be sufficiently accurate for the time scale estimation required here.

Further, the heat transfer Spalding number

$$B_T = \frac{C_p^g (T_\infty - T_d)}{L_v} \approx \frac{C_p^g (T_{ad} - T_d^s)}{L_v}, \quad (20)$$

600 is used instead of the mass transfer Spalding number  $B_d$  of Sec. 2, because the former can be better estimated without knowing the flow. In case of steady-state evaporation (as underlying the (diameter)<sup>2</sup>-law), either of the two transfer numbers can be used to calculate the evaporation constant  $K_v$ . The choice of the ambient temperature  $T_\infty \approx T_{ad}$  is not too sensitive due to the  $\ln(1 + B_T)$ -influence in Eqs. 18 and 19.  $T_d \approx T_d^s$  is a standard assumption, because 605 the droplets are first heated up until they reach the saturation temperature  $T_d^s$ . Subsequently, the heat flux from the surrounding hot gas to the droplet is taken up by the phase change and the droplet temperature remains fairly constant. Following common practice for first order estimations of adiabatic 610 flame temperature, the temperature-averaged value of  $C_p^g$  is based on the excess species  $N_2$  which is also barely affected by the chemical reaction.

The simple model for the maximum flame temperature  $\hat{T}_b^{\text{droplets}}$ , based on the comparison of evaporation and flame time scales, accounting for both dilution and cooling effect of water droplets, eventually reads

$$\hat{T}_b^{\text{droplets}} = T_0 + \frac{\overbrace{HY_{F,0} [1 - \min(\tau_f/\tau_v; 1) Y_W]}^{\text{dilution effect}}}{C_p^g} - \frac{\overbrace{L_v \min(\tau_f/\tau_v; 1) Y_W}^{\text{cooling effect}}}{C_p^g} \quad (21)$$

615 which reduces to

$$\hat{T}_b^{\text{premixed}} = T_0 + \frac{HY_{F,0}}{C_p^g} \equiv T_{ad} \quad (22)$$

for stoichiometric combustion of n-heptane and air without water addition ( $Y_W = 0$ ). The flame time scale  $\tau_f$  is defined as the residence time of droplets within the flame which has to account for thermal expansion and the droplet slip velocity. Accordingly, the residence time scale is approximated as  $\delta_{th}/((u_u + u_b)/2 - u_{\text{rel}}) \approx \delta_{th}/((u_u + u_u(1 + \tau))/2 - u_u) = \delta_{th}/(u_u \tau/2)$ , since the slip velocity  $u_{\text{rel}}$  620 is on the order of the unburned velocity  $u_u = S_L$  for the conditions investigated and since only the corresponding quantities of the gaseous premixed reference

case are known a-priori. Important time scales during flame-droplet interactions have also been discussed by Wang et al. [52]. Although the latent heat of vaporization of water ( $L_v = 2.258$  MJ/kg) is clearly smaller than the heating value of n-heptane ( $H = 44.7$  MJ/kg), this can be compensated with respect to the cooling effect by the fact that the water mass fraction  $Y_W$  can be clearly larger than the initial stoichiometric fuel mass fraction of  $Y_{F,0} = 0.0622$ . In the limit of complete droplet evaporation within the flame, i.e. representing the maximum dilution effect, the fuel mass fraction is lowered to  $Y_F = Y_{F,0}(1 - Y_W)$  because  $Y_{F,0} = m_F/m_0$ ,  $Y_F = m_F/(m_0 + m_W)$  and  $Y_W = m_W/(m_0 + m_W)$ . Assuming that the steam mass fraction can be described by  $Y_W^g \approx \min(\tau_f/\tau_v; 1) Y_W$ , the minimum-function in Eq. 21 assures the correct asymptotic behaviour in this limiting case.

The last step is to relate the maximum flame temperature  $\hat{T}_b^{\text{droplets}}$  to the laminar burning velocity  $S_L^{\text{droplets}}$  under the influence of droplets. In accordance with the present thermo-chemistry (Eq. 2), for which the dimensional fuel reaction rate magnitude reads

$$\dot{\omega}_F \propto \hat{\rho} B Y_F Y_O \exp\left(\frac{-E_{ac}}{R\hat{T}_b}\right), \quad (23)$$

an expression for the laminar burning velocity can be devised as

$$S_L = \sqrt{2 \alpha_{T_0} \frac{B}{1 + \tau} \frac{Y_{O,0}}{\beta^3} \exp\left(\frac{-E_{ac}}{R\hat{T}_b}\right)} \quad (24)$$

following the theory of high activation energy asymptotics [53]. Here,  $\hat{\rho}$ ,  $B$ ,  $E_{ac}$ ,  $R$  and  $\alpha_{T_0}$  denote the dimensional density, pre-exponential factor, activation energy, gas constant and thermal diffusivity of the unburned gas, respectively. Based on an Arrhenius-like expression, Eq. 24 reflects the fact that the chemical reaction is dominated by the highest temperature  $\hat{T}_b$  within the flame. It can be seen in Fig. 12 that the steam concentration  $Y_W^g$  at the leading edge of the flame (as indicated by the purple iso-contours of  $c$ ) is approximately zero and therefore the oxygen concentration  $Y_{O,0}$  on the unburned side of the flame is practically identical in the premixed reference case and the droplet cases. In case of small values of  $L_v$  (in contrast to the very high value corresponding to water) which

650 leads to pre-evaporation ahead of the flame, it may be questioned whether  $Y_{O,0}$  in Eq. 24 remains approximately independent of the droplets. The Zel'dovich number  $\beta = E_{ac}(\hat{T}_b - T_0)/(R\hat{T}_b^2)$  and heat release parameter  $\tau = (\hat{T}_b - T_0)/T_0$  incorporate additional temperature-related terms:

$$S_L = \sqrt{2 \alpha_{T_0} B \left( \frac{T_0}{\hat{T}_b} \right) \frac{Y_{O,0}}{(\hat{T}_b - T_0)^3} \left( \frac{R\hat{T}_b^2}{E_{ac}} \right)^3 \exp \left( \frac{-E_{ac}}{R\hat{T}_b} \right)} \quad (25)$$

which yields the simplified temperature-related proportionality

$$S_L \propto \sqrt{\frac{\hat{T}_b^5}{(\hat{T}_b - T_0)^3} \exp \left( \frac{-E_{ac}}{R\hat{T}_b} \right)} \approx \sqrt{\exp \left( \frac{-E_{ac}}{R\hat{T}_b} \right)} \hat{T}_b \quad (26)$$

655 since  $\hat{T}_b \gg T_0$ . From Eq. 26, one obtains

$$\frac{S_L^{\text{droplets}}}{S_L^{\text{premixed}}} = \sqrt{\exp \left[ \frac{E_{ac}}{R} \left( \frac{1}{\hat{T}_b^{\text{premixed}}} - \frac{1}{\hat{T}_b^{\text{droplets}}} \right) \right]} \frac{\hat{T}_b^{\text{droplets}}}{\hat{T}_b^{\text{premixed}}} \quad (27)$$

for the ratio of laminar burning velocities for purely gaseous premixed conditions and under the influence of droplets. The values corresponding to the gaseous premixed reference case are taken for the activation energy  $E_{ac}$  and gas constant  $R$ .

660 Quantitative results from the model equations and the corresponding DNS-based measurements are summarized in Table 3. The maximum normalized flame temperature  $T_b^{\text{droplets}} = (\hat{T}_b^{\text{droplets}} - T_0)/(T_{ad} - T_0)$ , as predicted by Eq. 21, can be readily compared to the most probable value of  $T$  on the burned gas side in the DNS as obtained from the PDFs of  $T$  in Fig. 10. The burning velocity reduction factor  $S_L^{\text{droplets}}/S_L^{\text{premixed}}$ , as predicted by Eq. 27, shall  
 665 be compared to the discrepancy between the black line representing the premixed reference case and the symbols representing the droplet cases in Fig. 7, i.e.  $(S_L^{\text{droplets}}/S_L^{\text{premixed}})_{\text{DNS}} \approx \min(\Omega^{\text{droplets}}/\Omega^{\text{premixed}})$ . From the comparison in Table 3, it can be concluded that the model works **reasonably well for**  
 670 **the conditions examined. In particular, the trends with respect to droplet size  $a_d/\delta_{th}$  and water loading  $Y_W$  are correctly captured by the model.** However, the model overestimates the burning velocity suppression effect for  $a_d/\delta_{th} = 0.02 -$

Case			$T_b^{\text{droplets}}$		$S_L^{\text{droplets}}/S_L^{\text{premixed}}$	
$a_d/\delta_{th}$	$Y_W$	Comment	DNS	Model	DNS	Model
0.04	0.1	droplet reference case	0.96	0.97	0.91	0.91
0.06	0.1	droplet size variation	0.97	0.98	0.96	0.95
0.02	0.1	droplet size variation	0.90	0.90	0.74	0.68
0.04	0.05	water loading variation	0.97	0.98	0.96	0.95
0.04	0.2	water loading variation	0.92	0.95	0.80	0.82

Table 3: DNS-based measurements and reduced-order model predictions of the maximum normalized flame temperature  $T_b^{\text{droplets}} = (\hat{T}_b^{\text{droplets}} - T_0)/(T_{ad} - T_0)$  and burning velocity reduction factor  $S_L^{\text{droplets}}/S_L^{\text{premixed}}$ , depending on the initial droplet size  $a_d/\delta_{th}$  and water loading  $Y_W$ ; initial  $u'/S_L = 4$  in all cases.

a case which results in strong deviations from the gaseous premixed reference conditions. This behaviour could be connected to the usage of a-priori available reference quantities like  $T_{ad}$  in Eq. 20 and  $\delta_{th}$  as required for  $\tau_f$  in Eq. 21. Hence, the proposed reduced-order model can be interpreted as a linear perturbation approach whose validity depends on the deviation from the reference state. The model is not intended to predict the quenching limit with respect to water addition. Further uncertainty is related to the estimation of the slip velocity  $u_{\text{rel}}$  (generally depending on the droplet size), which affects both the evaporation rate and the droplet residence time within the flame. It is also worth noting that the inlet and initial turbulence are characterized by the turbulence intensity according to  $u'/S_L$ , where  $S_L = S_L^{\text{premixed}}$  refers to the laminar burning velocity of the stoichiometric premixed flame without water droplets. In case of water droplet interaction, the turbulence intensity according to  $u'/S_L^{\text{droplets}}$  increases, since  $S_L^{\text{droplets}} < S_L^{\text{premixed}}$ . Hence, the relative importance of turbulence increases to a certain degree but this effect is counteracted by the dampening of flame-generated turbulence as discussed in Sec. 4.2.

A reduced-order model is necessarily a simplification of the complex real physics. For the conditions examined, the effect of turbulence on the evapora-

Case				$\Omega^{\text{droplets}}/\Omega^{\text{premixed}}$	
$u'/S_L$	$a_d/\delta_{th}$	$Y_W$	Comment	min	mean
4	0.04	0.1	droplet reference case	0.9117	0.9508
4	0.06	0.1	droplet size variation	0.9602	0.9768
4	0.02	0.1	droplet size variation	0.7424	0.8324
4	0.04	0.05	water loading variation	0.9592	0.9780
4	0.04	0.2	water loading variation	0.7997	0.8768
<hr/>					
0	0.04	0.1	droplet reference case	0.9024	0.9293
0	0.06	0.1	droplet size variation	0.9528	0.9673
0	0.02	0.1	droplet size variation	0.7072	0.7611
0	0.04	0.05	water loading variation	0.9543	0.9678
0	0.04	0.2	water loading variation	0.7682	0.8231

Table 4: DNS-based statistics of the burning rate reduction factor  $\Omega^{\text{droplets}}/\Omega^{\text{premixed}}$ , depending on the turbulence intensity  $u'/S_L$ , initial droplet size  $a_d/\delta_{th}$  and water loading  $Y_W$ .

tion rate is limited due to the combination of comparably small droplets and moderate turbulence intensities. This is demonstrated by the comparison of the burning rate statistics between the turbulent and the corresponding laminar cases, cf. Table 4, showing consistent but limited differences. The burning rate reduction by droplets is somewhat stronger, i.e. the values of  $\Omega^{\text{droplets}}/\Omega^{\text{premixed}}$  are consistently lower, in the laminar cases. There is no impediment in replacing the current evaporation law, Eq. 19, when elevated turbulence levels and/or larger droplet diameters are investigated. Independent of that, the base formulation of the model remains. There are different possibilities to account for the effect of turbulence on evaporation rates as reviewed by Birouk and Gökalp [54]. The effect of turbulence may also be reflected via the flame time scale  $\tau_f$ , i.e. the residence time of droplets within the flame. Another possibility would be to incorporate the eddy turn-over time  $t_{\text{turb}} = L_{11}/u'$  as a third characteristic time scale, such that the role of turbulent mixing (less dominant here but more important in technical applications) is also reflected in the model.

The Flamelet Generated Manifold (FGM) method [55] coupled with Artificially Thickened Flame (ATF) is a well-established modelling technique for the mean reaction rate term in the context of Large Eddy Simulations (LES) including premixed, partially-premixed, diffusion and spray flames. In the context of FGM for spray combustion [56, 57, 58, 59, 60], one needs to solve for the transport equations for Favre-averaged/filtered values of a suitably defined reacting scalar  $Y_{\text{RPV}}$  (e.g. a combination of mass fractions of major species) and mixture fraction  $\xi$ , which take the following generic form [60]:

$$\frac{\partial(\bar{\rho}\tilde{\psi})}{\partial t} + \frac{\partial(\bar{\rho}\tilde{\psi}\tilde{u}_j)}{\partial x_j} = \frac{\partial}{\partial x_j} \left[ \left( FE \frac{\bar{\mu}}{\text{Sc}_\psi} + (1 - \Phi) \frac{\mu_t}{\text{Sc}_{t,\psi}} \right) \frac{\partial\tilde{\psi}}{\partial x_j} \right] + \frac{E}{F} \bar{\omega}_\psi + \bar{S}_\psi, \quad (28)$$

where  $\psi = \{Y_{\text{RPV}}, \xi\}$ ,  $\tilde{u}_j$  is the  $j^{\text{th}}$  component of velocity,  $\bar{\mu}$  is the mean viscosity,  $\mu_t$  is the eddy viscosity,  $\text{Sc}_\psi$  is the Schmidt number of  $\psi$ ,  $\text{Sc}_{t,\psi}$  is the turbulent Schmidt number associated with  $\psi$ ,  $F$  is the flame thickening factor,  $\Phi$  is the flame sensor and  $E$  is the efficiency function. The source term  $\bar{\omega}_\psi$  originates only for  $Y_{\text{RPV}}$  and it is identically zero for  $\xi$ . The term  $\bar{S}_\psi$  arises due to two-way coupling between Eulerian and Lagrangian phases. The efficiency function  $E$  is a function of  $\Delta S_L/\alpha_{T_0}$  and  $u'_\Delta/S_L$  [61, 62], where  $u'_\Delta$  is the sub-grid velocity fluctuation and  $\Delta$  is the filter width. This suggests that the estimation of  $S_L$  plays a key role in the estimation of  $E$ , which is fundamentally important for the solution of Eq. 28, and thus can have pivotal importance in the fidelity of the FGM-ATM based modelling of premixed turbulent combustion in the presence of water droplets. Further discussion on this modelling is beyond the scope of this paper and will form the basis of further investigation.

## 5. Concluding remarks

Based on two-way coupled Euler-Lagrange discretization, carrier-phase DNS have been conducted in this work to shed light on the complex interaction of liquid water droplets and premixed hydrocarbon flames in a turbulent environment. An extensive parametric analysis (variation of droplet size, overall water

loading, turbulence intensity and latent heat of vaporization) revealed several insights into the underlying phenomena:

- 735 • Reductions of flame temperature and laminar burning velocity can be observed in the considered parameter range. The trends of flame thickness are opposite to the trends of burning velocity. According to the laws governing evaporation, a strongly non-linear influence of the droplet size has been observed, whereas the influence of water loading is fairly linear. This circumstance is particularly relevant to the design of engine applications or  
740 safety-related mitigation measures (e.g. involving aerodynamic breakup).
- Using realistic fluid properties of water, the cooling effect due to the enthalpy sink of evaporating droplets outweighs the dilution effect due to the local release of steam. The residence time of water droplets in the flame zone is a determining factor in this context.
- 745 • It is observed that turbulence plays an intricate role. First, droplet clustering, i.e. non-uniformity, in the unburned mixture facing the flame may potentially decrease the effectiveness of the droplets in reducing the overall burning rate as compared to laminar conditions. Second, the flame-generated turbulence is significantly diminished by the evaporating droplets  
750 and this has an additional effect on the turbulent burning velocity which is, to a large extent, determined by turbulent wrinkling of the flame surface. Turbulent mixing (of the localized enthalpy defect) can also be discerned from the probability distributions of temperature within the flame, thus underpinning the need for three-dimensional DNS for this kind of analysis.
- 755 • Different regimes of water droplet flame interaction can be distinguished based on the ratio of evaporation to flame time scales on the one hand and the ratio of mean droplet separation distance to flame thickness on the other hand. Owing to their low volatility, i.e. high latent heat of vaporization, realistic water droplets show a strong preference for a particular  
760 regime. By lowering the latent heat, the existence of a different regime has

been demonstrated. In such a case, the dilution effect gains in importance which leads to a significant perturbation of the flame surface.

- A simple model has been proposed to account for both the cooling and dilution effects with respect to flame temperature and laminar burning velocity. The underlying idea is based on a comparison of the time scales representing droplet evaporation and [the droplet residence time within the flame](#). The model can be used for preliminary estimations and may be further qualified for computationally more efficient approaches, like LES or RANS, where the interaction of individual droplets with the flame cannot be resolved explicitly.

To continue the work on this topic, a great variety of additional investigations are conceivable, e.g. on heterogeneous droplet size distributions (closer to technical applications), lean/rich equivalence ratios (thicker flames implying increased residence time of droplets within the flame) or different types of fuel like hydrogen (additional complexities due to flame instabilities in non-unity Lewis number flames). Regarding the regime diagram, it would be worthwhile to identify the boundaries between different regimes by scaling considerations or a larger number of simulations. To validate the simplified chemistry and to investigate the effects of water droplets on emissions, it will be necessary to repeat selected cases (due to high computational costs) using a detailed chemical reaction mechanism.

## Acknowledgments

This work was supported by a postdoc fellowship of the German Academic Exchange Service (DAAD).

## References

- [1] S. Lellek, Pollutant Formation in Premixed Natural Gas Swirl Flames with Water Injection, Ph.D. thesis, Technische Universität München, 2017.

- [2] L. Fan, C. Chong, K. Tanno, D. McGrath, Y. Zheng, S. Hochgreb, Measurement of the effect of water droplets on strained laminar flames using two-phase PIV, in: Proceedings of the Combustion Institute, Elsevier, 790 2020.
- [3] B. Dorschner, L. Biasiori-Poulanges, K. Schmidmayer, H. El-Rabii, T. Coloni, On the formation and recurrent shedding of ligaments in droplet aerobreakup, preprint arXiv:2003.00048 (2020).
- [4] G. Thomas, A. Jones, M. Edwards, Influence of water sprays on explosion development in fuel-air mixtures, Combustion Science and Technology 80 795 (1991) 47–61.
- [5] G. Thomas, On the conditions required for explosion mitigation by water sprays, Process Safety and Environmental Protection 78 (2000) 339–354.
- [6] K. Van Wingerden, B. Wilkins, The influence of water sprays on gas explosions. Part 1: water-spray-generated turbulence, Journal of Loss Prevention in the Process Industries 8 800 (1995) 53–59.
- [7] P. Zhang, Y. Zhou, X. Cao, X. Gao, M. Bi, Enhancement effects of methane/air explosion caused by water spraying in a sealed vessel, Journal of Loss Prevention in the Process Industries 29 805 (2014) 313–318.
- [8] C. Nicoli, P. Haldenwang, B. Denet, Premixed flame dynamics in presence of mist, Combustion Science and Technology 191 (2019) 197–207.
- [9] G. Thomas, M. Edwards, D. Edwards, Studies of detonation quenching by water sprays, Combustion Science and Technology 71 (1990) 233–245.
- [10] G. Jarsalé, F. Virot, A. Chinnayya, Ethylene–air detonation in water spray, 810 Shock Waves 26 (2016) 561–572.
- [11] A. Lazzarini, R. Krauss, H. Chelliah, G. Linteris, Extinction conditions of non-premixed flames with fine droplets of water and water/NaOH solutions, Proceedings of the Combustion Institute 28 (2000) 2939–2945.

- 815 [12] P. Arias, H. Im, P. Narayanan, A. Trouvé, A computational study of non-premixed flame extinction by water spray, *Proceedings of the Combustion Institute* 33 (2011) 2591–2597.
- [13] G. Koroll, S. Mulpuru, The effect of dilution with steam on the burning velocity and structure of premixed hydrogen flames, in: *21th Symposium (International) on Combustion*, 1988, pp. 1811–1819.
- 820 [14] G. Koroll, R. Kumar, E. Bowles, Burning velocities of hydrogen-air mixtures, *Combustion and Flame* 94 (1993) 330–340.
- [15] J. Chen, A. Choudhary, B. De Supinski, M. DeVries, E. Hawkes, S. Klasky, W. Liao, K. Ma, J. Mellor-Crummey, N. Podhorszki, R. Sankaran, S. Shende, C. Yoo, Terascale direct numerical simulations of turbulent combustion using S3D, *Computational Science & Discovery* 2 (2009) 015001.
- 825 [16] M. Klein, A. Herbert, H. Kosaka, B. Böhm, A. Dreizler, N. Chakraborty, V. Papapostolou, H. Im, J. Hasslberger, Evaluation of flame area based on detailed chemistry DNS of premixed turbulent hydrogen-air flames in different regimes of combustion, *Flow, Turbulence and Combustion* 104 (2019) 403–419.
- 830 [17] P. Libby, F. Williams, *Turbulent reacting flows*, Academic press, 1994.
- [18] E. Fernández-Tarrazo, A. Sánchez, A. Linan, F. Williams, A simple one-step chemistry model for partially premixed hydrocarbon combustion, *Combustion and Flame* 147 (2006) 32–38.
- 835 [19] S. Malkeson, N. Chakraborty, Statistical analysis of displacement speed in turbulent stratified flames: A direct numerical simulation study, *Combustion Science and Technology* 182 (2010) 1841–1883.
- [20] J. Reveillon, L. Vervisch, Analysis of weakly turbulent dilute-spray flames and spray combustion regimes, *Journal of Fluid Mechanics* 537 (2005) 317.
- 840

- [21] G. Ozel-Erol, J. Hasslberger, M. Klein, N. Chakraborty, A direct numerical simulation analysis of spherically expanding turbulent flames in fuel droplet-mists for an overall equivalence ratio of unity, *Physics of Fluids* 30 (2018) 086104.
- 845 [22] G. Ozel-Erol, J. Hasslberger, N. Chakraborty, Surface density function evolution in spherically expanding flames in globally stoichiometric droplet-laden mixtures, *Combustion Science and Technology* (2019) 1–21.
- [23] G. Ozel-Erol, J. Hasslberger, M. Klein, N. Chakraborty, A direct numerical simulation investigation of spherically expanding flames propagating in fuel droplet-mists for different droplet diameters and overall equivalence ratios, 850 *Combustion Science and Technology* 191 (2019) 833–867.
- [24] G. Ozel-Erol, J. Hasslberger, M. Klein, N. Chakraborty, Propagation of spherically expanding turbulent flames into fuel droplet-mists, *Flow, Turbulence and Combustion* 103 (2019) 913–941.
- 855 [25] G. Ozel-Erol, J. Hasslberger, N. Chakraborty, Statistics of two-phase coupling in turbulent spherically expanding flames in mono-sized fuel-droplet mists, *Combustion Science and Technology* (2020) 1–18.
- [26] K. Jenkins, R. Cant, Curvature effects on flame kernels in a turbulent environment, *Proceedings of the Combustion Institute* 29 (2002) 2023–860 2029.
- [27] A. Wandel, N. Chakraborty, E. Mastorakos, Direct numerical simulations of turbulent flame expansion in fine sprays, *Proceedings of the Combustion Institute* 32 (2009) 2283–2290.
- [28] A. Neophytou, E. Mastorakos, R. Cant, DNS of spark ignition and edge 865 flame propagation in turbulent droplet-laden mixing layers, *Combustion and Flame* 157 (2010) 1071–1086.
- [29] A. Wray, Minimal storage time advancement schemes for spectral methods, NASA Ames Research Center, California, Report No. MS 202 (1990).

- [30] T. Poinso, S. Lele, Boundary conditions for direct simulations of compressible viscous flows, *Journal of Computational Physics* 101 (1992) 104–129.
- [31] D. Wacks, N. Chakraborty, E. Mastorakos, Statistical analysis of turbulent flame-droplet interaction: a direct numerical simulation study, *Flow, Turbulence and Combustion* 96 (2016) 573–607.
- [32] D. Wacks, N. Chakraborty, Flow topology and alignments of scalar gradients and vorticity in turbulent spray flames: a direct numerical simulation analysis, *Fuel* 184 (2016) 922–947.
- [33] D. Wacks, N. Chakraborty, Flame structure and propagation in turbulent flame-droplet interaction: a direct numerical simulation analysis, *Flow, Turbulence and Combustion* 96 (2016) 1053–1081.
- [34] D. Wacks, N. Chakraborty, Statistical analysis of the reaction progress variable and mixture fraction gradients in flames propagating into droplet mist: a direct numerical simulation analysis, *Combustion Science and Technology* 188 (2016) 2149–2177.
- [35] S. Malkeson, D. Wacks, N. Chakraborty, Statistical behaviour and modelling of fuel mass fraction dissipation rate transport in turbulent flame-droplet interaction: A direct numerical simulation study, *Flow, Turbulence and Combustion* (2019) 1–30.
- [36] R. Rogallo, Numerical experiments in homogeneous turbulence, volume 81315, National Aeronautics and Space Administration, 1981.
- [37] J. Reveillon, L. Vervisch, Spray vaporization in nonpremixed turbulent combustion modeling: a single droplet model, *Combustion and Flame* 121 (2000) 75–90.
- [38] Y. Wang, C. Rutland, Effects of temperature and equivalence ratio on the ignition of n-heptane fuel spray in turbulent flow, *Proceedings of the Combustion Institute* 30 (2005) 893–900.

- [39] R. Sankaran, E. Hawkes, J. Chen, T. Lu, C. Law, Structure of a spatially developing turbulent lean methane–air Bunsen flame, *Proceedings of the Combustion Institute* 31 (2007) 1291–1298.
- [40] Y. Gao, N. Chakraborty, N. Swaminathan, Dynamic closure of scalar dissipation rate for large eddy simulations of turbulent premixed combustion: a direct numerical simulations analysis, *Flow, Turbulence and Combustion* 95 (2015) 775–802.
- [41] M. Boger, D. Veynante, H. Boughanem, A. Trouvé, Direct numerical simulation analysis of flame surface density concept for large eddy simulation of turbulent premixed combustion, in: *27th Symposium (International) on Combustion*, 1998, pp. 917–925.
- [42] M. Reeks, The transport of discrete particles in inhomogeneous turbulence, *Journal of Aerosol Science* 14 (1983) 729–739.
- [43] J. Young, A. Leeming, A theory of particle deposition in turbulent pipe flow, *Journal of Fluid Mechanics* 340 (1997) 129–159.
- [44] P. Gualtieri, F. Picano, G. Sardina, C. Casciola, Clustering and turbulence modulation in particle-laden shear flows, *Journal of Fluid Mechanics* 715 (2013) 134–162.
- [45] Q. Zhang, H. Liu, Z. Ma, Z. Xiao, Preferential concentration of heavy particles in compressible isotropic turbulence, *Physics of Fluids* 28 (2016) 055104.
- [46] L. Baker, A. Frankel, A. Mani, F. Coletti, Coherent clusters of inertial particles in homogeneous turbulence, *Journal of Fluid Mechanics* 833 (2017) 364–398.
- [47] S. Nishiki, T. Hasegawa, R. Borghi, R. Himeno, Modeling of flame-generated turbulence based on direct numerical simulation databases, *Proceedings of the Combustion Institute* 29 (2002) 2017–2022.

- [48] N. Chakraborty, M. Katragadda, R. Cant, Effects of Lewis number on turbulent kinetic energy transport in premixed flames, *Physics of Fluids* 23 (2011) 075109. 925
- [49] N. Chakraborty, M. Katragadda, R. Cant, Statistics and modelling of turbulent kinetic energy transport in different regimes of premixed combustion, *Flow, Turbulence and Combustion* 87 (2011) 205–235.
- [50] J. Furukawa, Y. Noguchi, T. Hirano, Investigation of flame generated turbulence in a large-scale and low-intensity turbulent premixed flame with a 3-element electrostatic probe and a 2-D LDV, *Combustion Science and Technology* 154 (2000) 163–178. 930
- [51] W. Ranz, W. Marshall, Evaporation from drops, *Chemical Engineering Progress* 48 (1952) 141–146.
- [52] Q. Wang, X. Zhao, M. Ihme, A regularized deconvolution model for sub-grid dispersion in large eddy simulation of turbulent spray flames, *Combustion and Flame* 207 (2019) 89–100. 935
- [53] F. Williams, *Combustion theory*, CRC Press, 2018.
- [54] M. Birouk, I. Gökalp, Current status of droplet evaporation in turbulent flows, *Progress in Energy and Combustion Science* 32 (2006) 408–423. 940
- [55] J. Van Oijen, A. Donini, R. Bastiaans, J. ten Thijsse Boonkcamp, L. De Goeij, State-of-the-art in premixed combustion modeling using flamelet generated manifolds, *Progress in Energy and Combustion Science* 57 (2016) 30–74.
- [56] G. Kuenne, F. Seffrin, F. Fuest, T. Stahler, A. Ketelheun, D. Geyer, J. Janicka, A. Dreizler, Experimental and numerical analysis of a lean premixed stratified burner using 1D Raman/Rayleigh scattering and large eddy simulation, *Combustion and Flame* 159 (2012) 2669–2689. 945
- [57] B. Fiorina, O. Gicquel, L. Vervisch, S. Carpentier, N. Darabiha, Approximating the chemical structure of partially premixed and diffusion coun-

- 950 terflow flames using FPI flamelet tabulation, *Combustion and Flame* 140  
(2005) 147–160.
- [58] A. Rittler, F. Proch, A. Kempf, LES of the Sydney piloted spray flame  
series with the PFGM/ATF approach and different sub-filter models, *Com-  
bustion and Flame* 162 (2015) 1575–1598.
- 955 [59] B. Franzelli, A. Vié, M. Boileau, B. Fiorina, N. Darabiha, Large eddy  
simulation of swirled spray flame using detailed and tabulated chemical  
descriptions, *Flow, Turbulence and Combustion* 98 (2017) 633–661.
- [60] F. Sacomano Filho, G. Kuenne, M. Chrigui, A. Sadiki, J. Janicka, A  
consistent artificially thickened flame approach for spray combustion using  
960 LES and the FGM chemistry reduction method: Validation in lean partially  
pre-vaporized flames, *Combustion and Flame* 184 (2017) 68–89.
- [61] O. Colin, F. Ducros, D. Veynante, T. Poinso, A thickened flame model  
for large eddy simulations of turbulent premixed combustion, *Physics of  
Fluids* 12 (2000) 1843–1863.
- 965 [62] F. Charlette, C. Meneveau, D. Veynante, A power-law flame wrinkling  
model for LES of premixed turbulent combustion, part i: non-dynamic  
formulation and initial tests, *Combustion and Flame* 131 (2002) 159–180.